Mapping deformation and dissipation during fracture of soft viscoelastic solid

Yuan Qi[1,†], Xueyu Li[2,3,†*], Sairam Pamulaparthi Venkata[4§], Xingwei Yang[1], Tao Lin Sun[5], Chung-Yuen Hui[3,4], Jian Ping Gong[2,3,6], Rong Long[1,*]

[1]Paul M. Rady Department of Mechanical Engineering, University of Colorado Boulder, Boulder, CO, 80309, USA

[2]Faculty of Advanced Life Science, Hokkaido University, Sapporo, 001-0021, Japan

[3]Soft Matter GI-CoRE, Hokkaido University, Sapporo 001-0021, Japan

[4]Field of Theoretical and Applied Mechanics, Sibley School of Mechanical and Aerospace Engineering, Cornell University, Ithaca, NY 14853, USA

[5]South China Advanced Institute for Soft Matter Science and Technology, South China University of Technology, Guangzhou, 510640, China

[6]Institute for Chemical Reaction Design and Discovery (WPI-ICReDD), Hokkaido University, Sapporo 001-0021, Japan

[†]These authors contribute equally to this paper.

[§]Current address: School of Mathematical and Statistical Sciences, University of Galway, University Road, Galway, H91 TK33, Ireland

*Corresponding authors: Xueyu Li and Rong Long

Email: lixueyu@sci.hokudai.ac.jp, rong.long@colorado.edu

Abstract

Energy dissipation around a propagating crack is the primary mechanism for the enhanced fracture toughness in viscoelastic solids. Such dissipation is spatially non-uniform and is highly coupled to the crack propagation process due to the history-dependent nature of viscoelasticity. We present an experimental approach to map the dissipation field during crack propagation in soft viscoelastic solid. Specifically, we track randomly distributed tracer particles to measure the evolving deformation field. The measured deformation field is then put into a nonlinear constitutive model to determine the dissipation field. Our methodology was used to investigate the deformation and dissipation fields around a propagating crack in a Polyampholyte (PA) hydrogel. The deformation field measurements allowed us to assess whether the commonly assumed translational invariance in viscoelastic fracture theories holds true in practical experiments. Furthermore, by combining the obtained deformation fields with a nonlinear viscoelastic model, we captured the complete

history of the dissipation field during crack propagation. We found that dissipation occurred even at material points that are a few millimeters away from the crack tip. The mapped dissipation field also enabled the separate determination of the intrinsic and dissipative components of fracture toughness for the viscoelastic hydrogel.

Keywords: fracture, viscoelasticity, particle tracking, dissipation, toughness.

1. Introduction

Viscoelastic solids represent a large class of synthetic or natural soft materials such as rubber (Creton and Ciccotti, 2016), pressure sensitive adhesives (Creton, 2003), and biological tissues (Humphrey, 2003). Unlike elastic solids which conserve energy upon deformation, viscoelastic solids dissipate the stored strain energy over time. It has been recognized that viscoelastic dissipation leads to significant enhancement in the fracture toughness Γ, i.e., the energy required per unit area of crack propagation (Gent, 1996; Knauss, 2015; Creton and Ciccotti, 2016). Specifically, energy supplied by the external loading, typically applied far away from the crack tip, needs to be transferred to the crack tip to drive crack propagation. In elastic solids, such energy transfer does not entail any loss. In viscoelastic solids, energy supplied by the external loading cannot be fully delivered to the crack tip. Consequently, Γ is larger than the energy per unit area necessary for material failure at the crack tip, known as the intrinsic fracture toughness Γ_0. The difference between them is the contribution due to viscoelastic dissipation: $\Gamma_D = \Gamma - \Gamma_0$. A key complication of this physical picture is the rate-dependent nature of Γ for viscoelastic solids. Because the dissipation at material points around a moving crack is sensitive to their stress and strain histories as the crack tip approaches and passes by, the dissipative term Γ_D (and hence Γ) depends on the crack propagation velocity, which is a hallmark of viscoelastic fracture.

Rate-dependent fracture toughness has been experimentally observed in a wide range of viscoelastic solids, examples including polyurethane elastomers (Knauss, 2015), synthetic rubber (Greensmith, 1964; Gent, 1996; Tsunoda et al., 2000) and pressure sensitive adhesives (Creton and Ciccotti, 2016). Moreover, the fracture toughness Γ measured at different crack propagation velocities and temperatures was found to follow the time-temperature superposition principle and can be correlated with the frequency-dependent storage modulus (Gent and Lai, 1994; Gent, 1996), further supporting the important role of viscoelasticity in fracture. Remarkably, Γ can be increased by 3 to 4 orders of magnitude as the crack propagation velocity increases (Gent and Lai, 1994; Knauss, 2015). Quantitative modeling of Γ_D is essential for understanding and predicting fracture in viscoelastic solids. However, achieving this task is not straightforward due to the intricate interplay between viscoelasticity, crack propagation, specimen geometry, and external loading (Knauss, 2015). A number of theories have been developed to predict the rate-dependence of Γ_D and Γ in

viscoelastic solids (Knauss, 1973; Schapery, 1975a, 1975b; Hui et al., 1992; de Gennes, 1996; Greenwood, 2004; Saulnier et al., 2004; Persson and Brener, 2005). All of these theories rely on two common assumptions as elaborated below.

- *Steady-state crack propagation*: this assumption states that the crack propagates at a constant speed and, more importantly, the stress and strain fields in the solid remain invariant in a translating coordinate system centered at the crack tip. This assumption allows one to convert the time derivative at a given material point to the spatial derivative at a given time, which is especially useful for calculating the rate of energy dissipation (de Gennes, 1996; Persson and Brener, 2005) and the crack opening displacement (Schapery, 1975a; Knauss, 2015).
- *Linear viscoelasticity*: this assumption allows one to apply the extended correspondence principle (Graham, 1968) for a propagating crack, and implies that the crack tip stress field in linear viscoelastic solid follows the same distribution as the linear elastic counterpart, e.g., the *K*-field for traction-free cracks (de Gennes, 1996; Persson and Brener, 2005).

In addition to these two assumptions, all theories need to model the fracture process occurring at the crack tip either by prescribing an intrinsic fracture toughness Γ_0 (de Gennes, 1996; Saulnier et al., 2004; Persson and Brener, 2005) or introducing a cohesive zone at the crack tip (Knauss, 1973; Schapery, 1975a, 1975b; Hui et al., 1992; Greenwood, 2004). The former approach focuses on integrating the bulk energy dissipation at different crack speeds, but requires a cut-off length to exclude a small region around the crack tip from the integral of dissipation (de Gennes, 1996; Persson and Brener, 2005). The latter approach focuses on determining the crack speed needed to satisfy the fracture criterion within the cohesive zone, in terms of the crack opening displacement (Knauss, 2015) or the intrinsic toughness Γ_0 (Schapery, 1975a; Knauss, 2015). Note that both approaches introduce a length scale, i.e., the cut-off length or the cohesive zone size, to reflect the size of the crack tip fracture process zone. These two approaches were shown to be essentially equivalent provided that the fracture process zone size can be considered as a fitting parameter (Ciavarella et al., 2021; Persson, 2021; Hui et al., 2022). The intrinsic toughness Γ_0 is typically assumed to be a material constant. For example, Γ_0 for crosslinked rubber can be estimated using the Lake-Thomas model (Lake and Thomas, 1967). However, recent studies suggest that the underlying mechanism for Γ_0 can become far more complex (Slootman et al., 2020) and can be altered by controlling the network structure

(Kim et al., 2021). Nevertheless, existing viscoelastic fracture theories have established analytical solutions relating the crack speed, the fracture toughness and the viscoelastic properties (e.g., creep function or dynamic modulus) (Hui et al., 2022), which are highly valuable for understanding the rate-dependent fracture in viscoelastic solids.

Despite the wide adoption, the two assumptions (i.e., steady-state crack propagation and linear viscoelasticity) pose limitations to the applicability of existing viscoelastic fracture theories. First, the steady-state assumption is not always satisfied in experiments (Knauss, 2015; Long and Hui, 2016). Non-steady-state crack propagation is commonly encountered in practice but is far less understood (Knauss, 2015). For example, crack propagation under cyclic loading is of fundamental importance towards understanding the fatigue behavior of viscoelastic solids (Lake and Lindley, 1964; Guo et al., 2022). Second, the linear viscoelasticity assumption results in a long-standing paradox, i.e., the cohesive zone size (or the crack tip cut-off length for the integral of dissipation) needs to be unrealistically small (i.e., in the sub-nanometer range) for the theories to fit experimental data (Gent, 1996; Knauss, 2015; Hui et al., 2022). It was suggested nonlinear viscoelasticity may be the key towards solving this paradox (Knauss, 2015; Guo et al., 2020). However, going beyond the steady-state and linear viscoelasticity assumptions is challenging. A central challenge lies in the lack of knowledge on how the nonlinear stress and strain fields evolve during non-steady-state crack propagation in viscoelastic solids. *Full-field measurement of the evolving deformation fields around a propagating crack in viscoelastic solids can provide key data towards addressing this challenge but is unavailable in the current literature.*

In this work, we present an experimental approach to characterize the time evolution of deformation fields during crack propagation in a highly stretchable viscoelastic hydrogel by tracking randomly distributed tracer particles (Qi et al., 2019; Lu et al., 2021). With the full-field and full-history data of deformation, we further demonstrate the mapping of dissipation and stress work during crack propagation using a nonlinear constitutive model of the hydrogel, based on which the two components of fracture toughness, Γ_0 and Γ_D, are separately determined. Specifically, we choose to use polyampholyte hydrogel (PA gel) (Sun et al., 2013) as a model material system and perform fracture tests using the strip geometry, which is also known as the pure shear configuration. The PA gel is selected for two reasons. First, it contains a large amount of dynamic, physical crosslinks and exhibits macroscopic viscoelasticity due to the dissociation and reformation of dynamic crosslinks

(Sun et al., 2015). Second, the high toughness of PA gel implies significant dissipation (Sun et al., 2017), and the large crack opening (Luo et al., 2014) during fracture enhances the signal-to-noise contrast in our measurement.

The plan of this paper is as follows. Section 2 below briefly summarizes the preparation of PA gel samples, the crack propagation experiments and the particle tracking method. In Section 3, we present the measured nonlinear deformation fields in the crack propagation experiments, followed by Section 4 where we use a constitutive model to determine the fields of stress work, dissipation, and free energy and to extract Γ_0, Γ_D and Γ. Conclusions are given in Section 5.

2. Materials and Methods

2.1 Gel sample preparation

Polyampholyte hydrogel (PA gel) was synthesized from anionic monomer sodium p-styrenesulfonate (NaSS) and cationic monomer methyl chloride quarternised *N,N*-dimethylamino ethylacrylate (DMAEA-Q) around the charge balance point, 2.5 M total monomer concentration, and 2.5 mM cross-linker N,N-methylenebis(acrylamide) concentration. The sample after synthesis was dialyzed in deionized water for at least two weeks with daily water exchanges. The water content and thickness of the sample were 45.7 wt% and ~1.7 mm, respectively. The detailed procedure of sample preparation was described in previous works (Sun et al., 2013; Ihsan et al., 2016). The sample had a characteristic dynamic relaxation peak around the angular frequency ω_c of 270 rad/s, which corresponds to a characteristic relaxation time of $\tau_c = 1/\omega_c$ = 0.004 s (Appendix A).

2.2 Crack propagation experiments

To perform crack propagation experiments, we used PA gel specimens in the form of thin sheets (50 mm × 50 mm × 1.7 mm). The thin sheet was mounted on two clamps of a tensile tester (Shimadzu Autograph AG-X with a 100 N load cell), and the distance between the clamps was 10 mm, which resulted in a strip area with width L_0 = 50 mm and height H_0 = 10 mm for testing. A crack (10 mm in length) was introduced at the edge of the thin sheet pure shear specimen along the width direction using a razor blade. Black glass beads (diameter ~ 200 μm) were spread on one

surface of the sample to serve as tracer particles for measuring the displacement and strain fields. These tracer beads were adhered to the gel surface during the entire course of crack propagation experiment and it was confirmed that they did not affect the tensile behavior of the gel (Appendix B). To prevent samples from dehydrating, a humidity chamber was installed on the tensile tester. Water vapor was constantly supplied in the chamber during each test. The two clamps of the tensile tester were separated to a preset stretch ratio λ_{hold} with an initial loading velocity of 0.01 mm/s, 0.5 mm/s or 10 mm/s and was then held fixed. Images of the samples were recorded during the crack propagation experiments. For slow initial loading (i.e., 0.01 mm/s), a digital camera (Canon 7D) was used to take images at a rate of 1 frame per 5 seconds. For fast initial loading (i.e., 0.5 or 10 mm/s), another digital camera (Basler acA4024-29uc) was used to take images at a higher rate of 10 frames per second. The spatial resolution of the images under our optical setup was ~ 15 μm per pixel. The temperature for the tests was kept constant at 24 ℃.

2.3 Particle tracking

For each image taken during the crack propagation experiment, we used the built-in function "*imfindcircles*" in MATLAB (Mathworks, Natick, MA, USA) to obtain the coordinates of centroid for each tracer bead. The Feature-Vector-Relaxation Method (FVRM) was adopted to track the tracer beads in two consecutive image frames (Feng et al., 2014). This method leverages the relative positions of neighboring beads around a tracer bead as a geometrical signature for tracking and is particularly suitable for tracer beads with random distributions. Specifically, FVRM compares the geometrical pattern formed by a target bead and its neighboring beads in the current image frame with a few candidate patterns in the next image frame. The pattern that best matches that in the current frame is selected, from which a pair of corresponding beads in the current frame and the next frame is identified. By linking the tracked pairs from the first to the last image frame, one can determine the trajectories of the tracer beads during the experiment.

2.4 Moving least square interpolation

Once displacements of the tracer beads were determined, we used the Moving Least Square (MLS) method to interpolate the measured displacement data of the tracer beads into a continuous field (Liu and Long, 2016). In a previous work, we have demonstrated that the particle tracking method was able to capture the displacement and deformation fields around a highly deformed

crack in a soft silicone elastomer with high resolution and accuracy (Qi et al., 2019). Specifically, to interpolate a scalar field function $g(\mathbf{X})$ where $\mathbf{X}$ is the coordinate vector of a material point, we start with a polynomial basis $\mathbf{P}(\mathbf{X})$ ($\mathbf{P}$ is a column vector) and the corresponding coefficients $\mathbf{a}(\mathbf{X})$ ($\mathbf{a}$ is a column vector) and construct the following interpolation function:

$$g(\mathbf{X}) = \mathbf{P}^T(\mathbf{X})\mathbf{a}(\mathbf{X}). \tag{1}$$

The difference between MLS and conventional polynomial interpolation is that the coefficients $\mathbf{a}(\mathbf{X})$ are also field functions. This feature enables the MLS method to accommodate complex fields using simple polynomial basis. For example, even with a linear basis, $\mathbf{P}(\mathbf{X}) = [1, X_1, X_2]^{\mathrm{T}}$, one can obtain a sophisticated field $g(\mathbf{X})$ due to the spatial variation in $\mathbf{a}(\mathbf{X})$. The coefficients $\mathbf{a}(\mathbf{X})$ are determined by minimizing the following least-square error function:

$$N = \sum_{k=1}^{n} \zeta(\mathbf{X} - \mathbf{d}_k)\left[\mathbf{P}^T(\mathbf{d}_k)\mathbf{a}(\mathbf{X}) - w_k\right]^2, \tag{2}$$

where $\mathbf{d}_{\mathrm{k}}$ are coordinate vectors of the tracer beads in the reference configuration, w_{k} is the measured data at the tracer beads, and $\zeta(\mathbf{X} - \mathbf{d}_{\mathrm{k}})$ is a weight function for the tracer beads that decays with the distance $|\mathbf{X} - \mathbf{d}_{\mathrm{k}}|$. We follow Qi et al. (2019) and adopt the linear basis $\mathbf{P}(\mathbf{X}) = [1, X_1, X_2]^{\mathrm{T}}$ and the following exponential weight function:

$$\zeta(\mathbf{X} - \mathbf{d}_k) = \begin{cases} \dfrac{\exp\left(1 - \left|\mathbf{X} - \mathbf{d}_k\right|^2 / r_c^2\right) - 1}{\exp(1) - 1} & \left|\mathbf{X} - \mathbf{d}_k\right| \le r_c \\ 0 & \left|\mathbf{X} - \mathbf{d}_k\right| > r_c \end{cases}. \tag{3}$$

The cut-off radius r_c was set to be twice the average of the ten smallest values of $|\mathbf{X} - \mathbf{d}_{\mathrm{k}}|$, i.e., twice the average distance to the ten closest tracer beads. This set of interpolation parameters was shown to provide accurate measurement for the crack tip displacement and strain fields in a soft elastomer (Qi et al., 2019). The MLS method was applied to the in-plane displacement components with w_{k} being the measured displacements of tracer beads. Strain fields can be obtained by taking spatial gradients of the interpolated displacement fields (Hall et al., 2012; Liu and Long, 2016).

3. Deformation Fields during Crack Propagation

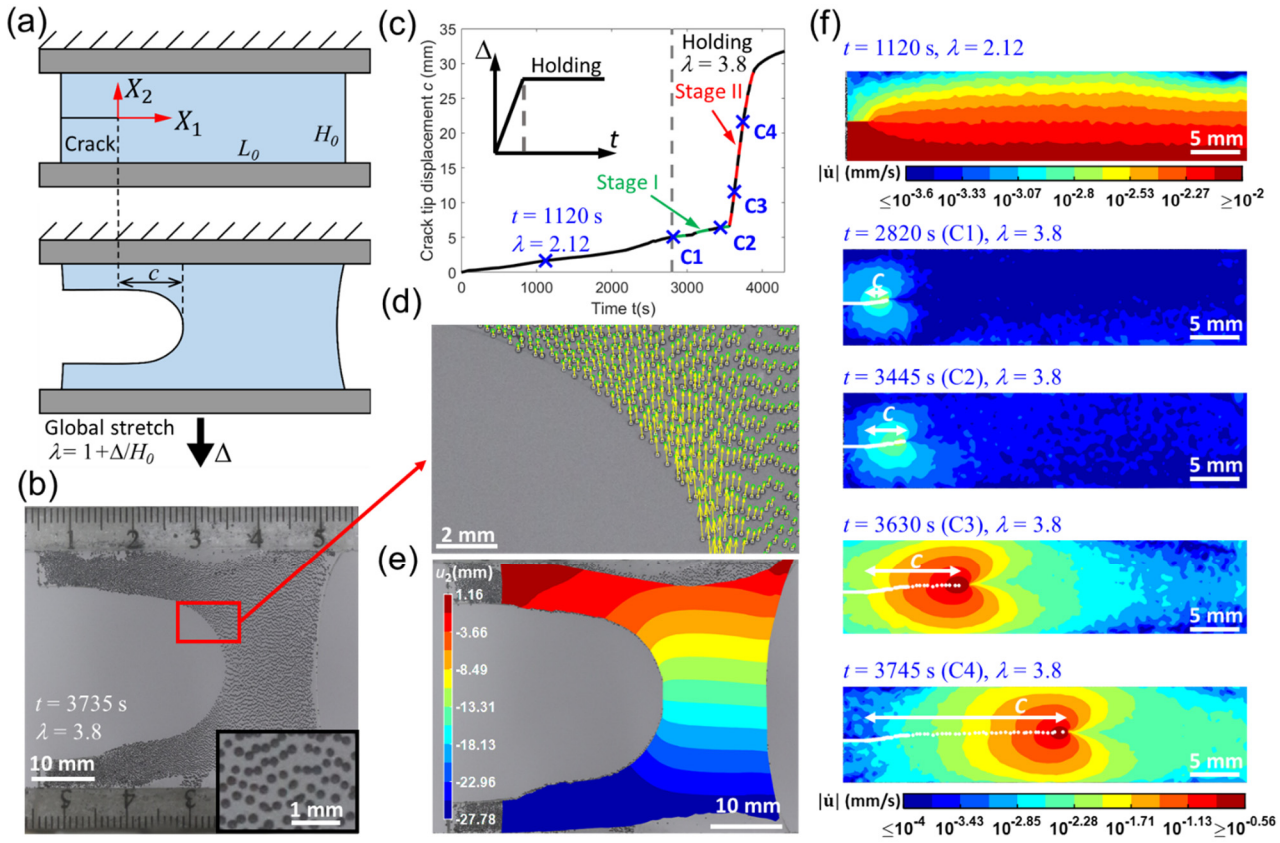

Figure 1. Crack propagation experiment and particle tracking. **(a)** Schematic of the pure shear specimen before and after loading, where c is the horizontal displacement of crack tip and λ is the global stretch ratio. **(b)** A representative image showing the deformed sample and tracer beads. **(c)** Crack tip displacement c versus time. The inset illustrates the loading history and the vertical dashed line marks when holding started. Two distinct stages with constant crack tip velocities can be identified and are denoted as Stage I and II. **(d)** Tracer particle displacements (yellow arrows) between two consecutive time frames (t = 3735 and 3740 s). **(e)** Contour plot of vertical displacement component u_2 shown in the deformed configuration (t = 3735 s) obtained by interpolating the tracer particle displacements. **(f)** Distribution of the velocity magnitude $|\dot{\mathbf{u}}|$ shown in the reference configuration at five different times (with the corresponding global stretch λ) marked in **(c)**. The initial crack is shown as a white line and the reference crack tip positions after the crack propagation started are shown as white dots. Results in **(b-f)** are obtained from the slow loading case ($\dot{\lambda}$ = 10^{-3} s^{-1} and λ_{hold} = 3.8)

3.1 Crack propagation

To put our results into perspective, we first briefly summarize the crack propagation experiments. Recall that all experiments were conducted using thin sheet samples with strip geometry as illustrated in Fig.1a (width L_0 = 50 mm, height H_0 = 10 mm, thickness B_0 = 1.7 mm and initial crack length = 10 mm). We set up a Cartesian coordinate system (Fig.1a) such that crack propagation was along the positive X_1 direction. With respect to this coordinate system, the top boundary of the sample was fixed, and the bottom boundary was separated from the top one with a constant velocity $\dot{\Delta}$ until the global stretch ratio $\lambda \equiv 1 + \Delta / H_0$ reached a prescribed value λ_{hold}. After that, the displacement Δ was held fixed while the crack propagation proceeded. We set the initial loading velocities to be $\dot{\Delta}$ = 0.01, 0.5 or 10 mm/s (corresponding to initial stretch rate: $\dot{\lambda}$ = 10^{-3}, 0.05 or 1 s^{-1}) and the prescribed stretch λ_{hold} to range from 3 to 5. These initial strain rates are much slower than the inverse of the characteristic relaxation time τ_c ($1/\tau_c \sim 270$ s^{-1}). Due to the extremely broad viscoelastic peak (Appendix A), the PA gel is in elastic regime at $\dot{\lambda}$ = 10^{-3} s^{-1} while it is in slightly viscoelastic regime at $\dot{\lambda}$ = 0.05 s^{-1}. Among the different combinations of $\dot{\lambda}$ and λ_{hold}, we chose two representative cases, i) $\dot{\lambda}$ = 10^{-3} s^{-1} and λ_{hold} = 3.8 or ii) $\dot{\lambda}$ = 0.05 s^{-1} and λ_{hold} = 3.8, to perform particle tracking. These two cases will be referred to as the slow loading and the fast loading case, respectively. As mentioned in Section 2.2, prior to perform particle tracking, black glass beads (diameter ~ 200 μm) were spread on one surface of the PA gel sheet to serve as tracer particles without altering its mechanical properties (Appendix B). During the experiment, the PA gel sample and the tracer beads were imaged by a digital camera at high resolution (pixel size ~ 15 μm). Note that λ_{hold} = 3.8 was selected as an intermediate value in the range of 3 to 5 to ensure that the speed of crack propagation was suitable for imaging. In addition, particle tracking was not performed for the fastest initial stretch rate of $\dot{\lambda}$ = 1 s^{-1}, since this rate resulted in similar crack propagation behaviors as those under slower initial stretch rate (e.g., $\dot{\lambda}$ = 10^{-3} s^{-1}), which will be discussed later in this section.

We use the slow loading case ($\dot{\lambda}$ = 10^{-3} s^{-1} and λ_{hold} = 3.8) as an example to describe our observations. This experiment spanned from t = 0 s when the initial loading started to t = 4340 s.

The global stretch λ first increased linearly with time and then was held after t = 2800 s when λ_{hold} = 3.8 was reached. A representative image of the sample at t = 3735 s is shown in Fig.1b. Note that the tracer beads can be clearly identified from the image (see the inset of Fig.1b). More images of the sample are given in Appendix C. To illustrate the extent of crack propagation, we extracted the horizontal component of the crack tip displacement, denoted as c (Fig.1a), and plotted it against the time t (Fig.1c). It should be emphasized that the crack tip displacement c does not only come from material separation due to crack propagation but can also be due to large deformation of the sample. This is evidenced by the fact that c began to increase as soon as the initial loading started at t = 0 s. However, after the global stretch was held fixed at t = 2800 s (i.e., "Holding" in Fig.1c), the contribution of large deformation to the crack tip displacement c should remain approximately constant. As a result, the slope dc/dt, defined as the *crack tip velocity* v, can be used as a measure for crack propagation during holding (i.e., after t = 2800 s). This will be confirmed in Section 3.3 where we determine the true crack extension.

The curve in Fig.1c exhibits a sudden change of slope during holding ($\lambda = \lambda_{hold}$ = 3.8). This sudden change occurred at t = 3565 s. Before that, the crack tip velocity was $v_I = 2.24\times10^{-3}$ mm/s. After t = 3565 s, the crack tip velocity jumped to a much higher value of $v_{II} = 8.80\times10^{-2}$ mm/s. Eventually the crack tip slowed down as it approached the right boundary of the PA gel sample. Remarkably, the nearly 40-fold increase from v_I to v_{II} occurred under a fixed displacement Δ (or equivalently, under a fixed stretch λ_{hold}). The fast loading case with $\dot{\lambda}$ = 0.05 s^{-1} and λ_{hold} = 3.8 exhibited a similar sudden crack acceleration (Fig.8 of Appendix D). In the following, the two stages of crack propagation with low and high crack tip velocities will be referred to as Stage I and Stage II (Fig.1c), respectively. Further experiments revealed that the two stages of crack tip velocity depend on the initial stretch rate $\dot{\lambda}$ and the fixed stretch λ_{hold} (Fig.9 of Appendix D). Specifically, using a much higher initial stretch rate ($\dot{\lambda}$ = 1 s^{-1}), we also observed the two stages of crack propagation and the sudden acceleration from Stage I to Stage II under different λ_{hold} (Fig.9b in Appendix D). It is interesting to note that the stretch rate of $\dot{\lambda}$ = 1 s^{-1} is in the strong viscoelastic regime as illustrated in Fig.5 of Appendix A. For this case, the crack tip velocities at the two stages are closer (Fig.9b of Appendix D) in comparison to those under the lower initial stretch rate of $\dot{\lambda} = 10^{-3}$ s^{-1} (Fig.9a of Appendix D). For both initial stretch rates (i.e., $\dot{\lambda} = 10^{-3}$ s^{-1}

or 1 s^{-1}), increasing λ_{hold} resulted in higher crack tip velocities in Stage I and Stage II crack propagation. Moreover, only Stage I crack propagation was observed if λ_{hold} is below a threshold, and only Stage II crack propagation was observed if λ_{hold} is above a threshold (see Fig.9 of Appendix D).

The sudden crack acceleration observed in our experiments has been reported for other hydrogels and is known as delayed fracture (Bonn et al., 1998; Wang and Hong, 2012; Tang et al., 2017; Bai et al., 2019). In particular, Tang et al. (2017) observed a sudden transition from slow to rapid crack propagation under a static displacement load in polyacrylamide gels that are nearly elastic. The Stage II crack propagation in our experiments is slower than that observed for polyacrylamide gels (Tang et al., 2017), presumably due to the viscoelasticity of PA gels. Delayed fracture was also observed in unnotched PA gel samples during creep test at constant tensile stress (Karobi et al., 2016). Note that delayed fracture occurs under a static displacement load, and therefore is different from the crack velocity transition under increasing displacement reported for elastomers (Tsunoda et al., 2000; Morishita et al., 2016). The underlying physical mechanism for the sudden crack acceleration is likely due to certain kinetic processes at the crack tip (Tang et al., 2017), which is not the focus of this work. Instead, we aim to understand how the two stages of crack propagation and the sudden acceleration affect the deformation and dissipation fields in the PA gel using the particle tracking data, as discussed in the following sections.

3.2 Displacement fields and true crack extension

The in-plane displacements of tracer beads were determined by first tracking them between consecutive time frames (see Fig.1d for an example) and then linking the tracer displacements over all time frames. The discrete displacement data at the tracer beads were interpolated into a continuous field using the MLS method detailed in Section 2.4. We follow the Lagrangian description of deformation and use the initial coordinates (X_1, X_2) of a material point as its identifier. Therefore, the in-plane displacement field can be expressed as a vector function $\mathbf{u}(X_1, X_2)$. An example of the displacement field is shown in Fig.1e in terms of the vertical component $u_2(X_1, X_2)$. The displacement field establishes a mapping between the initial

coordinates of a material point (i.e., X_1 and X_2) to its coordinates in the deformed configuration (i.e., $x_1 = X_1 + u_1$ and $x_2 = X_2 + u_2$). We also obtained the material velocity field $\dot{\mathbf{u}}(X_1, X_2)$ at each time frame using the incremental displacement field between two consecutive frames and the corresponding time increment. The velocity field can provide important data for understanding the viscoelastic behavior of PA gel during crack propagation. In Fig.1f we plot spatial distributions of the velocity magnitude $|\dot{\mathbf{u}}|$ for the slow loading case at five different time frames. All plots are shown in the initial configuration. The five time frames are marked in Fig.1c for reference. The latter four time frames at t = 2820 s, 3445 s, 3630 s or 3745 s occurred during holding ($\lambda = \lambda_{hold}$ = 3.8) and are denoted as C1, C2, C3 and C4, respectively. It can be seen that C1 to C2 and C3 to C4 represent two time durations in Stage I and Stage II, respectively.

The velocity fields in Fig.1f exhibit distinct patterns. At t = 1120 s, the PA gel was still under the initial loading and hence the velocity field exhibited a vertical gradient from the fixed top boundary to the moving bottom boundary. This gradient disappeared once holding started. Instead, the velocity field is concentrated at the crack tip due to the rapid local deformation. This is interesting given that the global stretch was held fixed. We attribute the concentrated velocity field at the crack tip to crack propagation. The sudden crack acceleration observed in Fig.1c is reflected in the substantially larger velocity magnitude in Stage II (e.g., C3 and C4) than that in Stage I (e.g., C1 and C2). It is worth noting that for a stationary crack in a linear viscoelastic solid (i.e., in the absence of crack propagation), the correspondence principle would imply that the velocity field should remain constant with time under a fixed displacement loading. However, as demonstrated by Wang et al. (2023), in a comparable PA gel system, time-dependent localized deformation near the crack tip can occur even for a stationary crack due to nonlinear viscoelasticity. Wang et al. (2023) proposed that, unlike in a linear viscoelastic solid where relaxation time remains unaffected by strain, in a nonlinear viscoelastic solid, relaxation time decreases as strain increases. Consequently, the material at the crack tip undergoes softening due to pronounced strain concentration. This allows for an increase in the velocity field at the crack tip while simultaneously experiencing a commensurate decrease further away from the crack tip.

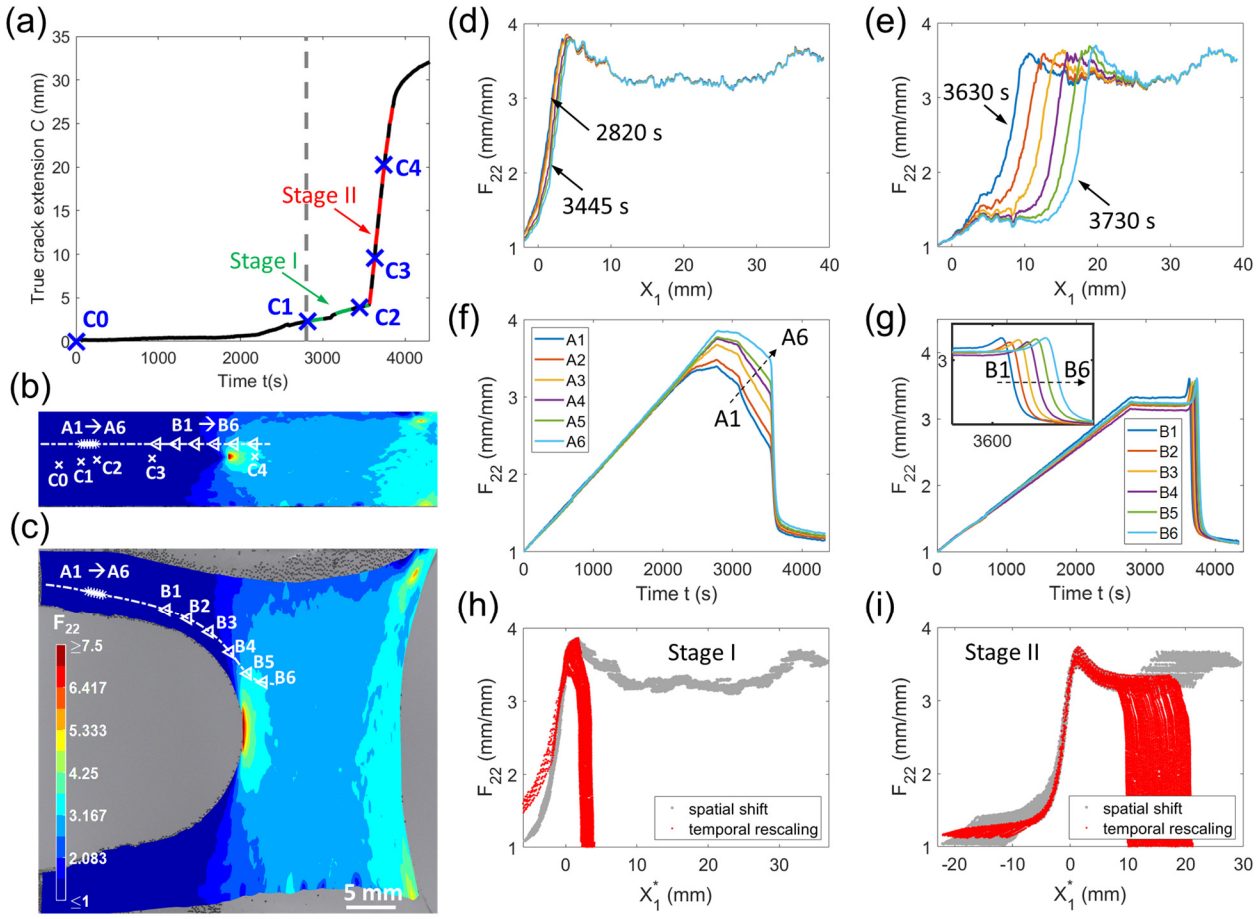

Figure 2. True crack extension and deformation field for the slow loading case ($\dot{\lambda} = 10^{-3}$ s^{-1} and $\lambda_{hold} = 3.8$). **(a)** True crack extension C versus time. The vertical dashed line indicates when holding started. **(b-c)** Distribution of F_{22} at $t = 3710$ s plotted in **(b)** the initial configuration and **(c)** the deformed configuration. In **(b-c)** the same color bar and scale bar are used. The reference crack tip positions at C0 ($t = 0$ s), C1 ($t = 2820$ s), C2 ($t = 3445$ s), C3 ($t = 3630$ s), and C4 ($t = 3745$ s) are marked in **(b)**. The initial crack tip C0 is located at $X_1 = X_2 = 0$, and C1-C4 occurred during holding ($\lambda = \lambda_{hold} = 3.8$). **(d-e)** Spatial distributions of F_{22} along the horizontal line ($X_2 = 2.14$ mm) at different times during holding in **(d)** Stage I ($t = 2820$ s to 3445 s with an equal increment of 125 s) and **(e)** Stage II ($t = 3630$ s to 3730 s with an equal increment of 20 s). **(f-g)** Histories of F_{22} at **(f)** A1-A6 and **(g)** B1-B6 on the horizontal line of $X_2 = 2.14$ mm. **(h-i)** Data points of spatial shift (grey) and temporal rescaling (red) for F_{22} during **(h)** Stage I and **(i)** Stage II.

The measured displacement fields also allow us to define the true crack extension as the length of crack trajectory in the initial configuration. The position of crack tip identified from each image is in the deformed configuration. Using the displacement field at each time frame, we mapped the crack tip position back to the initial configuration (Qi et al., 2019). The crack tip positions, after being mapped to the initial configuration, are illustrated in Fig.1f as white dots. They line up and form a trajectory of crack propagation. The length of this crack trajectory can only be increased by crack propagation, thereby removing the contribution of large deformation to the crack tip displacement c. It can be seen in Fig.1f that the crack trajectory slightly deviated from the expected propagation direction (i.e., along the X_1-axis), but mostly remained horizontal. Therefore, we formally define the true crack extension as the length of the crack trajectory projected to the X_1-axis and denote it as C (Fig.1f) to distinguish it from the crack tip displacement c.

The true crack extension C, when plotted against the time t in Fig. 2a, shows that crack propagation started at about t = 2000 s. Before that, the increase in crack tip displacement c (see Fig.1c) is primarily due to large deformation of the PA gel sample during the initial loading. Similar to Fig.1c, Fig.2a also features two stages of crack propagation with constant slopes after holding started. We define the time derivative of true crack extension, $\dot{C} \equiv dC/dt$, as the *crack extension speed* V. For Stage I and II, the crack extension speed is found to be $V_I = 2.67\times10^{-3}$ mm/s and $V_{II} = 9.24\times10^{-2}$ mm/s, respectively. Interestingly, both V_I and V_{II} are slightly larger than their counterparts in terms of the crack tip velocity, i.e., $v_I = 2.24\times10^{-3}$ mm/s and $v_{II} = 8.80\times10^{-2}$ mm/s. This is because the crack extension speed V and the crack tip velocity v are defined by the same segment of crack propagation between two consecutive time frames, but the segment length used for V and v is measured in the initial and deformed configurations, respectively. As will be shown in Section 3.3, the region directly ahead of the crack tip was subjected to a slight horizontal contraction (i.e., along the X_1-axis). This explains why v is smaller than V. The small difference between them suggests that the crack tip velocity v, which is much easier to determine in experiments, can be used as a measure for crack propagation under fixed displacement loading.

3.3 Deformation field and translational invariance

The strain field during crack propagation can be obtained by taking spatial gradients of the displacement field $\mathbf{u}(X_1, X_2)$. Because of the nonlinearity associated with large deformation, we use the deformation gradient tensor **F** to represent the strain field. The tensor **F** is defined as

$$\mathbf{F} = \nabla_{\mathbf{X}}\mathbf{u} + \boldsymbol{\delta} \ , \tag{4}$$

where $\boldsymbol{\delta}$ is the identity tensor. Since the deformation fields in our samples are primarily governed by plane stress condition, we focus on the four in-plane components of **F**. With the full history of the displacement field $\mathbf{u}(X_1, X_2)$, we have access to all four components of **F** at any material point (X_1, X_2) and any time frame, as shown in the Supplementary Movie S1 (see Appendix G for description) obtained for the slow loading case ($\dot{\lambda} = 10^{-3}$ s^{-1} and $\lambda_{hold} = 3.8$). As expected for Mode-I cracks, the fields of F_{11} and F_{22} are approximately symmetric about the opened crack, while the fields of F_{12} and F_{21} are anti-symmetric. In particular, F_{22} is the dominant component of **F**, especially near the crack tip, since it reflects the stretching deformation along the X_2-direction (i.e., the direction of loading) (Long and Hui, 2015). In contrast, F_{11} is close to but less than 1 ahead of the crack tip, indicating a slight contraction along the X_1-direction.

The severely blunted crack and the large deformation near the crack tip clearly show that our experiments are beyond the regime of linear viscoelasticity. Next, we examine if the steady-state assumption is satisfied for the two stages of crack propagation observed in our experiments. In addition to constant crack extension speed V, the steady-state assumption also requires translational invariance, i.e., the stress and strain fields in a translating coordinate system centered at the crack tip should remain unchanged. To facilitate discussion, we set the origin of the fixed coordinate system X_1 - X_2 at the initial crack tip (Fig.1a). Because the trajectory of crack propagation is along the X_1-direction, the translating coordinate system is given by $X_1^* = X_1 - C$ and $X_2^* = X_2$. Translational invariance can be mathematically stated as

$$\mathbf{F}\left(X_1, X_2, t\right) = \mathbf{F}^*\left(X_1^*, X_2^*\right) = \mathbf{F}^*\left(X_1 - C(t), X_2^*\right), \tag{5}$$

where $\mathbf{F}^*$ is a time-independent tensorial function of X_1^* and X_2^*. To examine if Eq. (5) is satisfied, we choose to focus on the dominant component F_{22} ($\equiv 1+\partial u_2/\partial X_2$). Spatial distribution of F_{22} at a representative time (t = 3710 s) during holding ($\lambda = \lambda_{hold}$ = 3.8) is plotted in Fig.2b-2c in the initial and deformed configurations, respectively.

We monitor the data of F_{22} along a horizontal line in the reference configuration (X_2 = 2.14 mm) and perform two ways of data processing: spatial shift and temporal rescaling. For the spatial shift, we extracted the spatial distribution of F_{22} along the horizontal line at different times within Stage I and II (Fig.2d-2e). At each time, we implemented the coordinate shift $X_1^* = X_1 - C(t)$ using the true crack extension C in Fig.2a and replotted F_{22} versus X_1^* in Fig.2h-2i (grey dots). For the temporal rescaling, we consider the time evolution of F_{22} at given material points. Specifically, we selected two time intervals during holding ($\lambda = \lambda_{hold}$ = 3.8) from Fig.2a: C1-C2 for Stage I and C3-C4 for Stage II. The corresponding spatial ranges are defined by the reference crack tip locations at C1 to C4 (Fig.2b). Within each spatial range, we selected six evenly spaced material points along the same horizontal line (A1-A6 for Stage I and B1-B6 for Stage II as illustrated in Fig.2b-2c). The full histories of F_{22} at A1-A6 and B1-B6 were extracted (Fig.2f-2g). Since X_1 is fixed for a given material point, an increasing time t implies decreasing X_1^*, i.e., the material point is getting closer to the crack tip due to crack propagation. Therefore, for each material point we calculated X_1^* over time using $X_1^* = X_1 - C(t)$, and replotted F_{22} versus X_1^* in Fig.2h-2i (red dots). The temporal rescaling effectively flipped and rescaled the time for the F_{22} history.

If Eq. (5) is satisfied, data points from spatial shift and temporal rescaling should collapse onto a master curve given by the function $\mathbf{F}^*(X_1^*, X_2^*)$. However, such a collapse was not found for either Stage I or II, implying that neither stage exactly satisfies the steady-state assumption. Further examination of Fig.2h-2i shows that the spatial shift and temporal rescaling agreed well near the crack tip ($X_1^* = 0$). Discrepancies mainly occurred ahead of ($X_1^* > 0$) and behind ($X_1^* < 0$) the crack tip. Ahead of the crack tip, the spatial shift gave an approximately constant F_{22} except near

the right edge. In contrast, the temporal rescaling recorded the initial linear increase of F_{22} with time (Fig.2f-2g), which deviates from the spatial shift data. Such deviation is more pronounced for Stage I (Fig.2h) since it immediately followed the initial loading. In Stage II, F_{22} at a point remained constant during holding until the crack tip approached it (Fig.2g). This segment of constant F_{22} agreed well with the spatial shift data. Behind the crack tip, the discrepancy is due to the slow creep after the crack tip passed a material point. For example, in Stage I (Fig.2h), the spatial shift data show that F_{22} decayed to ~ 1 behind the crack tip (e.g., $X_1^* = -5.8$ mm), which is expected since material behind the crack tip was not subjected to any deformation. However, temporal rescaling gave a higher F_{22} (~ 1.5) at the same location. This is because the strain at a material point was not immediately recovered after sudden unloading. This creep effect is also observed in Stage II (Fig.2i), causing the scattering of data points for X_1^* ranging roughly from −20 mm to −10 mm.

The deformation field data show that neither Stage I or II strictly satisfies the translation invariance despite the constant crack extension speed. Similar analysis was performed for the fast loading case ($\dot{\lambda} = 0.05$ s^{-1} and $\lambda_{hold} = 3.8$) (see Supplementary Movie S2). In this case, the sudden acceleration between two stages of crack propagation was also observed (Appendix E). The crack extension speed increased by 33 folds from Stage I ($V_I = 1.42\times10^{-2}$ mm/s) to Stage II ($V_{II} = 0.47$ mm/s). We also found that both stages do not exactly satisfy the translation invariance in Eq. (5) (see Fig.10 in Appendix E). The breakdown of translational invariance implies that the deformation history experienced by a material point is no longer solely governed by the advective effect of crack propagation. Non-advective effects caused by external loading and specimen geometry may also affect viscoelastic dissipation and hence the toughness Γ. Next, we examine the energetics associated with the two stages of crack propagation.

4. Energy Dissipation and Fracture Toughness

4.1 Constitutive model and stress field

We use the data of deformation gradient **F** obtained from particle tracking to further quantify the viscoelastic dissipation during crack propagation. To proceed, a constitutive model is required to calculate the stress at a material point from the history of deformation gradient **F** for the PA gel. We adopt a recently developed constitutive model to capture the nonlinear viscoelastic behaviors of polyampholyte (PA) gels with both chemical and physical crosslinks (Venkata et al., 2021). The detailed mathematical formulation is given in Appendix F. Here we briefly describe the underlying physical picture assumed by this constitutive model.

Following the methodology established for modeling the dual crosslinked polyvinyl alcohol (PVA) hydrogel (Long et al., 2014; Guo et al., 2016), the constitutive model adopted here divides the polymer network of PA gel into a permanent network formed by chemical crosslinks and a transient network formed by physical crosslinks. If breaking and reforming of the physical crosslinks are suppressed, the mechanical responses of both networks follow the same hyperelastic model, specifically the Yeoh model (Yeoh, 1993). However, unlike the permanent network of which the chain density is constant, the transient network evolves over time due to the breaking and reforming of physical crosslinks. To capture this effect, the detachment and reattachment of chains in the transient network are tracked by following the breaking and reforming kinetics of physical crosslinks. Since newly reattached chains should be in the relaxed configuration, chains in the transient network only experience a segment of the macroscopic deformation history ranging from the time of their reattachment to the current time. Consequently, the strain energy stored in the transient network is governed by a convolution integral of the macroscopic deformation history and the chain reattachment rate. By summing the strain energies from the elastic permanent network and the transient network, one can determine the total strain energy at any time under a prescribed deformation history. Equations for the stresses can then be derived from the total strain energy using the Coleman-Noll procedure in continuum mechanics (Holzapfel, 2000).

Unlike phenomenological models based on the spring-dashpot representation, e.g., the quasilinear viscoelastic model (Simo, 1987), the model adopted here has a clear physical picture and is developed within a thermodynamic framework. Therefore, it allows unambiguous determination of the free energy (or strain energy) density Ψ, which may not be available in the quasilinear model. In addition, this model incorporates strain-dependent kinetics for the physical crosslinks and has been shown to be in good agreement with the data of uniaxial tensile tests with

various loading history (Venkata et al., 2021). To calibrate the model parameters for the PA gel used in our experiments, we performed loading-unloading cyclic tensile tests and fitted the model to the tensile data (Fig.3a and Appendix F).

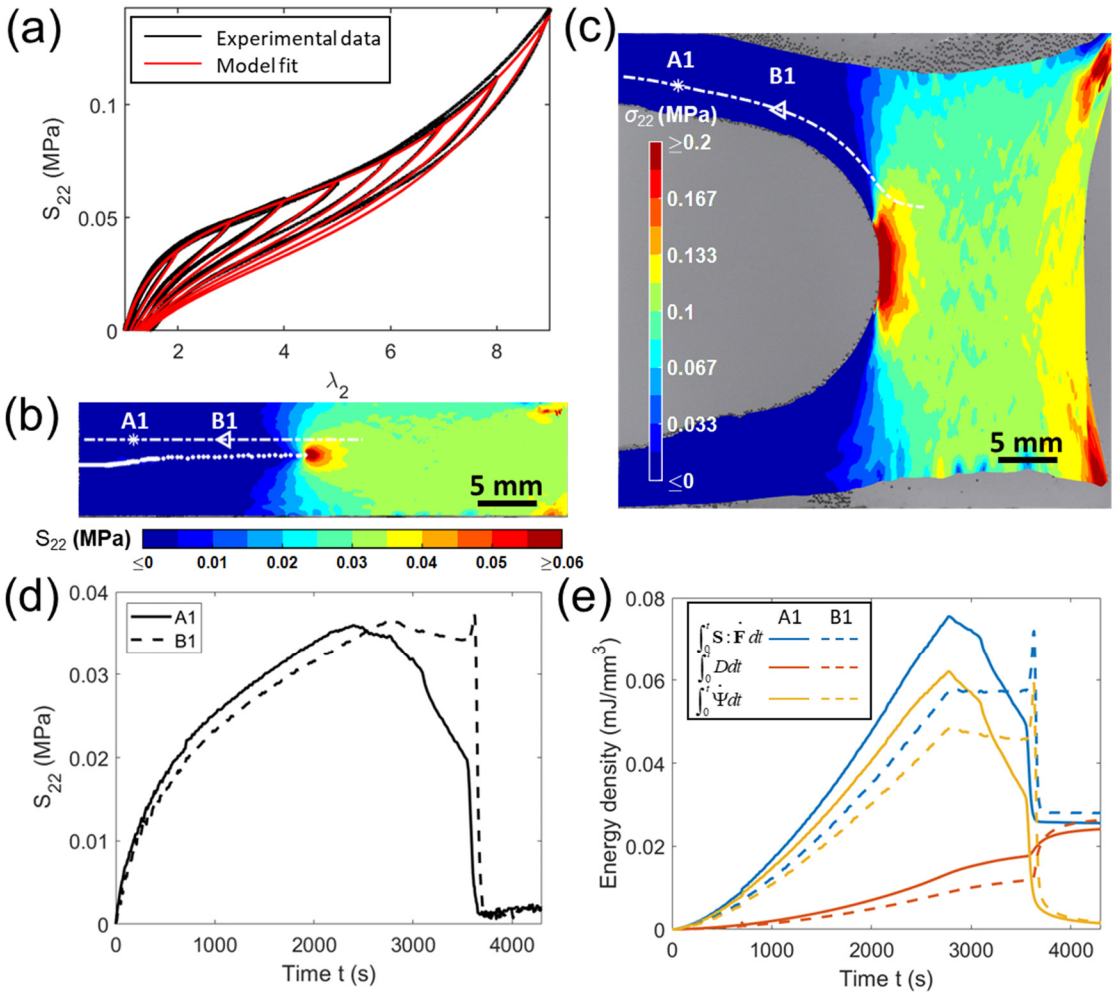

Figure 3. Determining stress and energy from constitutive model. **(a)** Calibration of constitutive model by fitting independent cyclic uniaxial tension data with a stretch rate of 0.042 s^{-1}. **(b)** Distribution of the nominal stress component S_{22} in the reference configuration at $t = 3710$ s during holding ($\lambda = \lambda_{hold} = 3.8$) for the slow loading case ($\dot{\lambda} = 10^{-3}$ s^{-1} and $\lambda_{hold} = 3.8$). **(c)** Distribution of the true stress σ_{22} in the deformed configuration corresponding to **(b)**. **(d)** Stress history in terms of S_{22} at two representative material points A1 and B1 calculated using the experimentally obtained deformation gradient **F** and the constitutive model. **(e)** Accumulated densities of stress work (blue), dissipation (red), and free energy (yellow) at A1 (solid lines) and B1 (dashed lines).

We apply the plane stress condition and the calibrated constitutive model to calculate the in-plane components of the first Piola Kirchhoff stress tensor **S** from the history data of **F**. An example of the resulting stress field is shown in Fig.3b using the dominating component S_{22}. The true stress tensor $\boldsymbol{\sigma}$ (also known as the Cauchy stress) can then be calculated from **S** and **F** using $\boldsymbol{\sigma} = \mathbf{S}\mathbf{F}^{\mathrm{T}} / \det(\mathbf{F})$. Figure 3c shows a distribution of the true stress component σ_{22} in the deformed configuration corresponding to Fig.3b. The magnitude of σ_{22} is several times larger than S_{22} ahead of the crack tip, which is attributed to thinning of the sample under stretch. Through this process, we can obtain the full stress history at any given material point, as shown in Fig.3d for two representative points A1 and B1 marked in Fig.2b.

4.2 Stress work and dissipation

Equipped with the constitutive model, we can now determine dissipation. To formally define dissipation, we start with the Clausius-Duhem inequality for solids (Holzapfel, 2000):

$$\mathbf{S} : \dot{\mathbf{F}} - \dot{e} + \theta\dot{\eta} - \frac{1}{\theta}\mathbf{q} \bullet \nabla_{\mathbf{X}}\theta \geq 0, \tag{6}$$

where **S** is the first Piola-Kirchhoff stress tensor, **F** is the deformation gradient tensor, e is the internal energy per unit volume, θ is the temperature, η is the entropy per unit volume, **q** is the heat flux and $\nabla_{\mathbf{X}}$ is the gradient operator in the initial configuration. All quantities are defined with respect to the initial configuration and the dot denotes material time derivative. We assume isothermal condition given the thin sheet geometry of the PA gel sample and the constant ambient temperature (i.e., room temperature). Under isothermal condition, the strain energy density Ψ given in Appendix F is recognized as the Helmholtz free energy density. Using the isothermal condition and the relation $\Psi = e - \theta\eta$, we can simplify Eq. (6) to

$$D = \mathbf{S} : \dot{\mathbf{F}} - \dot{\Psi} \geq 0, \tag{7}$$

where D is the dissipation power density, i.e., energy dissipated per unit time and per unit reference volume.

Equation (7) states that the dissipation power density D must be non-negative. If $\mathbf{S}:\dot{\mathbf{F}} > 0$ at a material point, the environment surrounding it is doing positive work to this point. A part of this work is stored as the free energy by increasing Ψ, and the rest is dissipated. On the other hand, if $\mathbf{S}:\dot{\mathbf{F}} < 0$, the material point is doing positive work to its environment. Such work must come from the stored free energy Ψ, implying that $\dot{\Psi} < 0$. In this case, Eq. (7) dictates that $\left|\dot{\Psi}\right| \geq \left|\mathbf{S}:\dot{\mathbf{F}}\right|$. Finally, even if $\mathbf{S}:\dot{\mathbf{F}} = 0$, $\dot{\Psi}$ can be negative (i.e., the stored free energy decreases) which leads to dissipation. This case corresponds to viscoelastic relaxation under fixed $\mathbf{F}$ (i.e., $\dot{\mathbf{F}} = 0$). It can be shown that the constitutive model summarized in Appendix F satisfies the inequality in Eq. (8) using the Coleman-Noll procedure (Holzapfel, 2000). Physically, the dissipation power density D is attributed to the detachment of temporary chains: once a temporary chain is broken, the strain energy stored on this chain is dissipated. The newly reattached chains carry zero strain energy and thus do not contribute to the total free energy.

The double inner product $\mathbf{S}:\dot{\mathbf{F}}$ ($\equiv \sum_{j=1}^{2}\sum_{i=1}^{2} S_{ij}\dot{F}_{ij}$) can be directly evaluated using the histories of $\mathbf{S}$ and $\mathbf{F}$, while Ψ is defined by constitutive model (Appendix F) and thus can also be evaluated using the history of $\mathbf{F}$. Therefore, we can evaluate the accumulated densities of stress work, dissipation and free energy within any material point by performing time integrals of $\mathbf{S}:\dot{\mathbf{F}}$, D and $\dot{\Psi}$ as shown in Fig.3e for two representative material points. Videos showing time evolution of the F_{22}, $\dot{F}_{22}$, D and $\int_0^t D dt$ fields are provided for the slow loading case (Supplementary Movie S3) and fast loading case (Supplementary Movie S4).

4.3 Energy balance analysis

To relate the densities of stress work, dissipation and free energy to fracture toughness, we start with the following energy balance equation for isothermal, quasi-static crack propagation, which was derived based on the first and second laws of thermodynamics (Qi et al., 2018):

$$\int_{\Omega} \mathbf{T}\bullet\frac{d\mathbf{u}}{dt}d\Omega - \int_{\Pi}\dot{\Psi}d\Pi - \Gamma_0\frac{d\Xi}{dt} = \int_{\Pi} D d\Pi, \tag{8}$$

where Π is the volume of a solid body, Ω is the boundary surface, $\mathbf{T}$ is the traction vector, $\mathbf{u}$ is the displacement vector, Γ_0 is the intrinsic fracture toughness (formally defined as the Helmholtz free energy required to propagate the crack per unit area), Ξ is the crack surface area measured in the reference configuration and D is the dissipation power density ($D \geq 0$). Substituting the definition of D in Eq. (7) into Eq. (8), we obtain

$$\int_{\Omega} \mathbf{T} \bullet \frac{d\mathbf{u}}{dt} d\Omega - \int_{\Pi} \mathbf{S} : \dot{\mathbf{F}} d\Pi = \Gamma_0 \frac{d\Xi}{dt}. \tag{9}$$

Equation (9) is a statement of mechanical energy balance in the solid. In particular, for a volume of solid that does not contain any crack tip, the term associated with Γ_0 vanishes and Eq. (9) recovers the mechanical energy balance equation for solids under quasi-static deformation (i.e., no inertial effects) and no body forces (Holzapfel, 2000).

The first integral on the left-hand side of Eq. (9) represents the external power applied to the solid. In our experiment, both Stage I and Stage II of crack propagation occurred during the holding period in which the boundaries of the strip sample were either traction free or held fixed. Therefore, the external power is zero during the two stages of crack propagation. Using the plane stress condition and the identity that $d\Xi / dt = VB_0$ where V is the crack extension speed (i.e., $V \equiv dC/dt = \dot{C}$ and C is the true crack extension length) and B_0 is the sample thickness (both measured in the reference configuration), we find that Eq. (9) becomes

$$-\iint_{A} \mathbf{S} : \dot{\mathbf{F}} dA = \Gamma_0 \dot{C}, \tag{10}$$

where A is surface domain of the gel sample on the X_1-X_2 plane.

Equation (10) shows that the intrinsic toughness Γ_0 is related to the integral of stress power density $\mathbf{S} : \dot{\mathbf{F}}$, which is directly specified by the constitutive model. In contrast, the definition of total toughness Γ and dissipative toughness Γ_D depends on how the stored energy and dissipation are defined, which may vary between constitutive models. For example, in phenomenological spring-dashpot models for viscoelasticity (e.g., generalized Maxwell model with Prony series), the

definition of stored energy and dissipation may not be available. The constitutive model adopted here has a well-defined free energy density Ψ, thus allowing us to clearly define Γ and Γ_{D} as

$$-\iint_A \dot{\Psi} dA = \Gamma V = \Gamma \dot{C}, \tag{11}$$

$$\iint_A D dA = \Gamma_{\mathrm{D}} V = \Gamma_{\mathrm{D}} \dot{C}. \tag{12}$$

Note that Eq. (11) is consistent with the definition of energy release rate under fixed displacement boundary condition. By combining eqs. (7), (10), (11) and (12), we recover the decomposition: $\Gamma_{\mathrm{D}} = \Gamma - \Gamma_0$. We reiterate that the values of Γ and Γ_{D} depend on the interpretation of the stored energy and dissipation for an inelastic material, while Γ_0 in Eq. (10) only depends on the stress power $\mathbf{S} : \dot{\mathbf{F}}$ and thus is well-defined even if the constitutive model lacks a thermodynamic interpretation.

To determine Γ_0, Γ_{D} and Γ from the fields of $\mathbf{S} : \dot{\mathbf{F}}$, D and $\dot{\Psi}$, we introduce the accumulated stress work $U_S = \int_0^t \left(\iint \mathbf{S} : \dot{\mathbf{F}} dA \right) dt$, the accumulated dissipation $U_D = \int_0^t \left(\iint D dA \right) dt$, and the total free energy $U_E = \int_0^t \Psi dt$. Based on Eq. (10)-(12), we have

$$-\dot{U}_S = \Gamma_0 \dot{C}, \quad \dot{U}_D = \Gamma_D \dot{C}, \text{ and } -\dot{U}_E = \Gamma \dot{C}. \tag{13}$$

Recognizing that $\dot{C} = dC / dt$, we rewrite Eq. (13) as

$$\Gamma_0 = -\frac{\dot{U}_S}{\dot{C}} = -\frac{dU_S}{dC}, \quad \Gamma_D = \frac{\dot{U}_D}{\dot{C}} = \frac{dU_D}{dC}, \text{ and } \Gamma = -\frac{\dot{U}_E}{\dot{C}} = -\frac{dU_E}{dC}. \tag{14}$$

Therefore, Γ_0, Γ_{D} and Γ are given by the absolute values of the slopes of U_S versus C, U_D versus C and U_E versus C curves, respectively. This method of determining Γ_0, Γ_{D} and Γ does not rely on the translational invariance condition and thus is also valid for non-steady state crack propagation. It should be noted that when integrating for U_S, U_D and U_E, we removed a small area behind the initial crack tip to reduce computational cost, because this area did not undergo any deformation and hence $\mathbf{S} : \dot{\mathbf{F}}$, D and $\dot{\Psi}$ are all zero in this area (Appendix H).

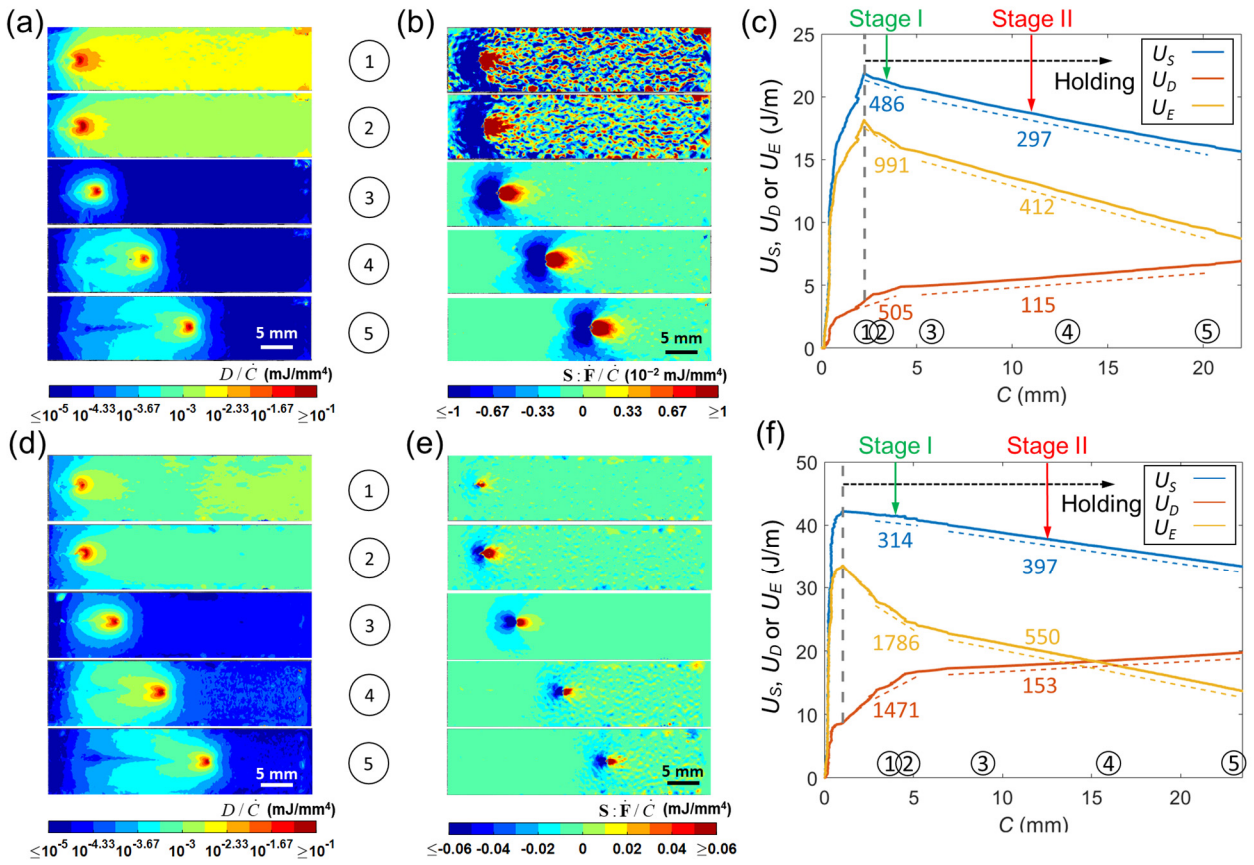

Figure 4. Dissipation and stress work during crack propagation. **(a-c)** Results for the slow loading case ($\dot{\lambda} = 10^{-3}$ s^{-1} and $\lambda_{hold} = 3.8$): **(a)** distributions of $D/\dot{C}$ and **(b)** distributions of $\mathbf{S}:\dot{\mathbf{F}}/\dot{C}$ at five different times (①: 2995 s; ②: 3245 s, ③: 3585 s, ④: 3665 s; ⑤: 3745 s) during holding ($\lambda = \lambda_{hold} = 3.8$), and **(c)** history of the total accumulated stress work U_S, dissipation U_D and free energy U_E in terms of the crack extension C. **(d-f)** Results for the fast loading case ($\dot{\lambda} = 0.05$ s^{-1} and $\lambda_{hold} = 3.8$): **(d)** distributions of $D/\dot{C}$ and **(e)** distributions of $\mathbf{S}:\dot{\mathbf{F}}/\dot{C}$ at five different times (①: 150.3 s; ②: 252.1 s, ③: 307.2 s, ④: 323.0 s; ⑤: 337.8 s) during holding ($\lambda = \lambda_{hold} = 3.8$), and **(f)** history of the total accumulated stress work U_S, dissipation U_D and free energy U_E in terms of the crack extension C. In **(c)** and **(f)**, the numbers (unit: J/m^2) represent the values of Γ_0 (blue), Γ_D (red) and Γ (yellow) obtained from slopes of the U_S, U_D and U_E data, respectively. The segments used for linear fitting are illustrated by dashed lines. The crack extensions corresponding to the snapshots in **(a-b)** and **(d-e)** are marked in **(c)** and **(f)**.

4.4 Toughness

The energy balance analysis in Section 4.3 paves the way for separately determining Γ_D and Γ_0 from experiments. Distributions of $D/\dot{C}$ and $\mathbf{S}:\dot{\mathbf{F}}/\dot{C}$ at five different snapshots are plotted for the slow loading case (Fig. 4a-4b) and the fast loading case (Fig. 4d-4e). The areal integrals of $D/\dot{C}$ and $\mathbf{S}:\dot{\mathbf{F}}/\dot{C}$ over the gel sample surface give Γ_D and Γ_0, respectively. We adopted a log-scale for the color map of $D/\dot{C}$ to better illustrate its distribution, while for $\mathbf{S}:\dot{\mathbf{F}}/\dot{C}$ we had to use a linear scale since it can be negative. By integrating $\mathbf{S}:\dot{\mathbf{F}}$, D and $\dot{\Psi}$ over the gel sample surface and over time, we obtained U_S, U_D and U_E and plotted them as functions of the true crack extension C (Fig. 4c and 4f). Recall that, by Eq. (14), the absolute values of slopes of $U_S(C)$, $U_D(C)$ and $U_E(C)$ versus C after holding started are equal to Γ_0, Γ_D and Γ, respectively.

The slow and fast loading cases share a number of interesting behaviors in the distributions of $D/\dot{C}$ and $\mathbf{S}:\dot{\mathbf{F}}/\dot{C}$. First, although all plots of the $D/\dot{C}$ fields are highly concentrated towards the crack tip, during Stage I the entire area ahead of the crack tip makes considerable contribution to the total dissipation power (Snapshot 1 and 2 in Fig.4a and 4d). This is attributed to the slow crack extension speed in Stage I, so that stress relaxation occurring in areas far ahead of the crack tip can still accumulate over time and lead to non-negligible dissipation per unit length of crack extension. Second, during Stage II the dissipation power mainly comes from a region translating with the crack tip (Snapshot 3, 4 and 5 in Fig.4a and 4d). The size of this region is not microscopic but is on the order of a few millimeters (see Fig.4a and 4d). However, the shape of this region kept evolving over time, especially behind the crack tip, which is caused by the development of a creep region behind the crack tip, as discussed earlier for Fig.2i. In addition, as Stage II proceeded (Snapshot 4 and 5 in Fig.4a and 4d), the dissipation region became confined by the top and bottom boundaries, suggesting that the dissipation field could be further expanded if the sample height H_0 was increased. Third, unlike $D/\dot{C}$, the $\mathbf{S}:\dot{\mathbf{F}}/\dot{C}$ fields (Fig.4b and 4e) feature a localized region near the crack tip. Specifically, the stress power density $\mathbf{S}:\dot{\mathbf{F}}$ is positive ahead of the crack tip where material points experienced loading, and is negative behind the crack tip where material points experienced unloading. The localized region of $\mathbf{S}:\dot{\mathbf{F}}/\dot{C}$ translated with the crack tip and maintained a nearly constant shape. This observation suggests that Γ_0, which is the areal integral

of the $\mathbf{S}:\dot{\mathbf{F}}/\dot{C}$ field, is approximately the same in Stage I and Stage II, even though these two stages have substantially different crack extension speed. Note that the large fuzzy pattern in Snapshot 1 and 2 of $\mathbf{S}:\dot{\mathbf{F}}/\dot{C}$ in Fig.4b are because the low crack speed $\dot{C}$ (= 2.67×10^{-3} mm/s) during Stage I amplified the noises in $\mathbf{S}:\dot{\mathbf{F}}$ far ahead of the crack tip.

Despite the nuanced behaviors in the $D/\dot{C}$ field, the total accumulated dissipation U_D still exhibited an approximately linear relation to the crack extension C (see Fig.4c and 4e). This is because U_D was dominated by the contribution from the crack tip given the log-scale color bar in Fig.4a and 4d. However, the slope $\Gamma_{\mathrm{D}} = dU_D/dC$ decreases significantly from Stage I to Stage II, which is attributed to the relaxation in the entire area ahead of the crack tip during holding (Snapshot 1 and 2 in Fig.4a and 4d). Such decrease from Stage I to Stage II is also found for the slope $\Gamma = -dU_E/dC$. In contrast, the slope $\Gamma_0 = -dU_S/dC$ remained approximately the same. The Γ_0, Γ_{D} and Γ determined by linearly fitting segments of the curves in Fig.4c and 4e are summarized in Table 1. In comparison to the steep drop in Γ_{D} and Γ from Stage I to Stage II, Γ_0 exhibits a much narrower range of ~ 300-486 J/m^2.

Table 1. Crack extension speeds and toughness values for the two stages of crack propagation in the slowing loading case ($\dot{\lambda}$ = 10^{-3} s^{-1} and λ_{hold} = 3.8) and the fast loading case ($\dot{\lambda}$ = 0.05 s^{-1} and λ_{hold} = 3.8).

	Slow loading case: Initial loading rate $\dot{\lambda} = 10^{-3}$ s^{-1} Holding stretch λ_{hold} = 3.8		Fast loading case: Initial loading rate $\dot{\lambda} = 0.05$ s^{-1} Holding stretch λ_{hold} = 3.8	
	Stage I	Stage II	Stage I	Stage II
Crack speed $\dot{C}$ (mm/s)	2.67×10^{-3}	9.24×10^{-2}	1.42×10^{-2}	0.47
Γ_0 (J/m^2)	486	297	314	397
Γ_{D} (J/m^2)	505	115	1471	153
Γ (J/m^2)	991	412	1786	550

The Γ_0 found in our experiments is comparable to or even larger than the corresponding Γ_D, except for Stage I of the fast loading case. This is consistent with comparison between the initial stretch rate $\dot{\lambda}$ and the inverse of characteristic relaxation time of the PA gel ($1/\tau_c \sim 270$ s^{-1}), i.e., $\dot{\lambda}$ for the slow loading case (10^{-3} s^{-1}) and the fast loading case (0.05 s^{-1}) falls into the elastic and the slightly viscoelastic regime of the PA gel (see Fig.5 in Appendix A). Therefore, the crack speeds in our experiments are not high enough to generate significant viscoelastic dissipation. This observation motivates future experiments with much higher $\dot{\lambda}$ and crack speeds, which can be practically difficult (e.g., high-speed imaging) and might require testing at lowered temperatures. Moreover, our computation for the stress work and dissipation relies on the constitutive model described in Appendix F. This model assumes the chemical crosslinks are permanent and hence never break. Effectively, it means that the chemical crosslinks can only break within the fracture process zone at the crack tip. However, recent experiments suggest that bond scission may occur in a non-localized manner beyond the crack tip (Slootman et al., 2020). If the chemical crosslinks in our PA gel also break away from the crack tip, a more sophisticated constitutive model will be needed to account for the additional dissipation caused by the breaking of chemical crosslinks.

We emphasize that Γ_0 is the intrinsic toughness for a propagating crack, as defined through the energy balance analysis in Eq. (9). Physically it describes the energy per unit area necessary to break bonds and create new surfaces at the crack tip. This definition should be distinguished from the fracture toughness of crack growth initiation, Γ^{init}, which is defined based on the critical stretch λ_c measured at the onset of growth for a stationary crack (Long and Hui, 2016). For purely elastic solids Γ_0 and Γ^{init} are equivalent, but for inelastic solids their relation is not yet well understood (Long and Hui, 2016). In particular, although Γ^{init} can be measured for viscoelastic solids, it may depend on the loading history and hence is not necessarily a material constant (Long and Hui, 2016). Nevertheless, given that Γ^{init} is often reported in the literature as a measure for the fracture resistance of soft gels, it is of interest to compare Γ^{init} and Γ_0 for the PA gel. As detailed in Appendix I, we measured Γ^{init} using both notched and unnotched PA gel samples with the same loading rates as our crack propagation experiments (i.e., $\dot{\lambda} = 10^{-3}$ s^{-1} or 0.05 s^{-1}). Since the PA gel

is viscoelastic, the mechanical work during the loading branch is not fully stored in the gel, thereby motivating us to use the unloading branch to obtain the stored strain energy (Mayumi et al., 2016; Zhang et al., 2022). The resulting Γ^{init} was found to be dependent on the unloading rate. Therefore, we set the unloading rate to be either the same as or much faster (i.e., 1.5 s^{-1}) than the loading rate and obtained a range of Γ^{init} for each loading rate. Specifically, Γ^{init} is 233~435 J/m^2 for loading rate $\dot{\lambda} = 10^{-3}$ s^{-1} and 404~566 J/m^2 for loading rate $\dot{\lambda} = 0.05$ s^{-1} (Table 3 in Appendix I). These values are close to the values of Γ_0 in Table 1.

5. Conclusions

This work presents an experimental study on the deformation and dissipation fields during crack propagation in a highly stretchable viscoelastic hydrogel. In our experiments, the crack first propagated at a low speed (Stage I) and then suddenly accelerated to a high speed (Stage II), which occurred in the absence of additional external work (i.e., under a fixed displacement loading). By tracking randomly distributed tracer particles deposited on the gel sample surface, we obtained the history of the in-plane displacement and deformation fields in the gel sample during crack propagation. The full-history and full-field data of the deformation gradient tensor were combined with a nonlinear viscoelastic constitutive model, from which we determined the powers of dissipation and stress work at each material point, thereby separating Γ_0 and Γ_D from the total toughness Γ. In contrast to the large difference in Γ_D between the two stages, Γ_0 was found to be in a smaller range of 300 ~ 486 J/m^2, thereby providing a measurement for the intrinsic toughness for crack propagation in the PA gel.

Apart from determining intrinsic toughness, we have also mapped the viscoelastic dissipation field around a propagating crack. Our results showed that dissipation can occur at material points that are a few millimeters away from the crack tip. Moreover, we observed the evolution of dissipation field during crack propagation and its confinement by the sample boundary, which suggests that the crack tip dissipation zone may depend on the loading history and the sample geometry (i.e., both shape and size). Unlike previous studies on the crack tip dissipation zone in viscoelastic fracture (de Gennes, 1996; Saulnier et al., 2004; Hui et al., 2022), which have been

limited to the theoretical level and rely on the assumptions of steady-state crack propagation and linear viscoelasticity, our method is based on the experimentally measured deformation field and can be extended to soft thin-sheet samples with any geometries, crack trajectories and loading histories, as long as an accurate constitutive model is available to capture the nonlinear viscoelasticity of the underlying solid. For example, our method can be applied to obtain useful insights towards how the sample dimensions, initial crack length and loading history affect crack propagation in soft viscoelastic solids.

Looking forward, the experimental method presented in this work can serve as a general tool for characterizing the evolution of nonlinear strain fields during crack propagation in soft viscoelastic solids. Experimental efforts in this direction will establish the foundation for new theories beyond the assumptions of steady-state crack propagation and linear viscoelasticity. The combination of non-steady state crack propagation and nonlinear viscoelasticity can open the door to new solution space unexplored by existing theories.

Acknowledgements

Y.Q, X.Y. and R.L. acknowledge funding support from the National Science Foundation USA through a CAREER award under Grant Number CMMI-1752449. X.L. and J.P.G. acknowledge funding support from JSPS KAKENHI under Grant Number JP22K20521 and JP22K21342. C.Y.H. and S.P.V. acknowledge funding supported from the National Science Foundation USA under Grant Number CMMI-1903308. Y.Q., X.L., R.L. and J.P.G. conceived the idea and designed the study. X.L. synthesized samples and performed fracture experiments and mechanical tests. Y.Q. and X.Y. carried out image analysis and data processing. S.P.V. and C.Y.H. developed and calibrated the constitutive model. All authors discussed and interpreted the results. Y.Q., X.Y. and R.L. drafted the manuscript and all authors revised it.

Appendix A. Viscoelastic behavior of the PA gel

The viscoelastic behavior of the PA gel is characterized by dynamic rheological test (ARES rheometer, Rheometric Scientific Inc.). A frequency sweep from 0.05 to 100 Hz was performed at a shear strain of 0.1% at temperatures from 0.1 to 95 °C. By following the principle of time-temperature superposition, master curves of storage modulus (G'), loss modulus (G'') and loss factor (tan δ) were constructed at a reference temperature of 25 ℃ (Fig.5). The angular frequency for the peak of tan δ (ω_c = 270 rad/s) gives a characteristic relaxation time of $\tau_c = 1/\omega_c = 0.004$ s.

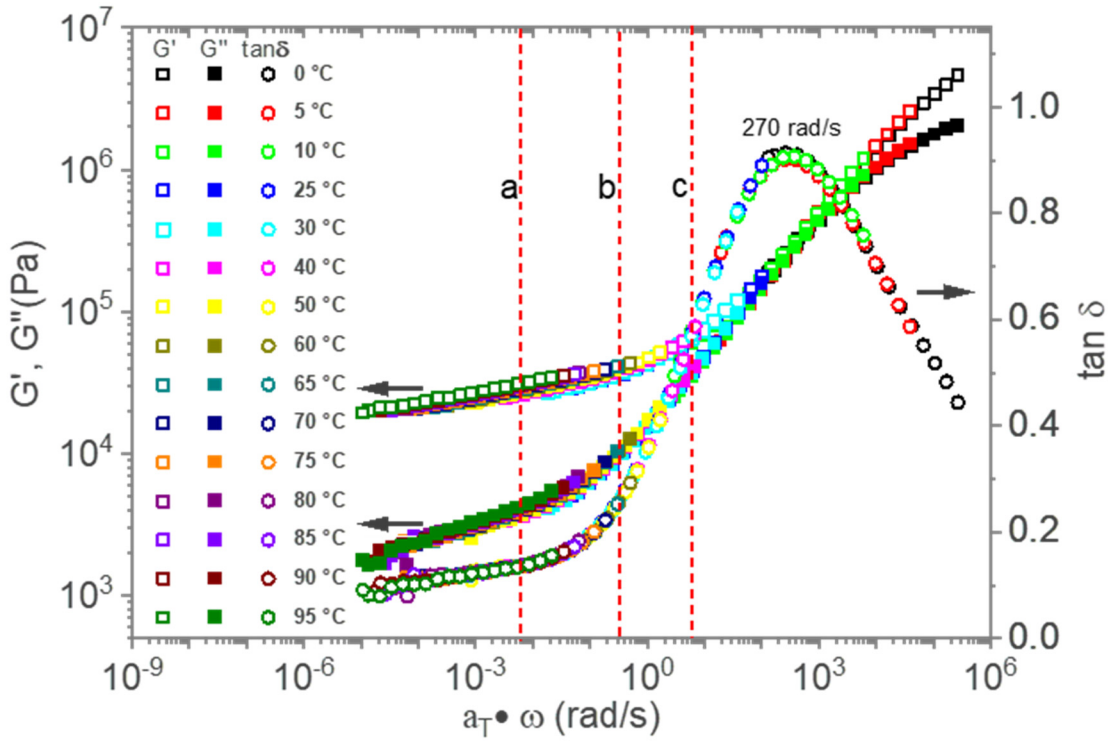

Figure 5. Constructed master curves for frequency dependence of storage modulus (G'), loss modulus (G''), and loss factor (tan δ) at a reference temperature of 25 ℃. a_T is the shift factor. Extremely broad viscoelastic peak is observed, and the dynamic relaxation peak is found at the angular frequency of ~ 270 rad/s. A recent work (Li et al., 2023) demonstrated that the stretch rate $\dot{\lambda}$ was correlated to the angular frequency ω by $\omega = 2\pi\dot{\lambda}$ through comparing the norm of the complex shear modulus versus the angular frequency ω from rheology test and the Young's modulus E versus $2\pi\dot{\lambda}$ from uniaxial tensile test. The three vertical dotted lines indicate the angular frequencies at which $\omega = 2\pi\dot{\lambda}$ for (a) $\dot{\lambda} = 10^{-3}$ s^{-1} (b) $\dot{\lambda} = 0.05$ s^{-1} and (c) $\dot{\lambda} = 1$ s^{-1}.

Appendix B. Effects of tracer beads on mechanical property

We performed uniaxial tensile tests using polyampholyte (PA) gel samples with or without the tracer beads deposited on the sample surface, as shown in Fig.6. The data suggest that the tracer beads on the surface of PA gel do not affect its mechanical property.

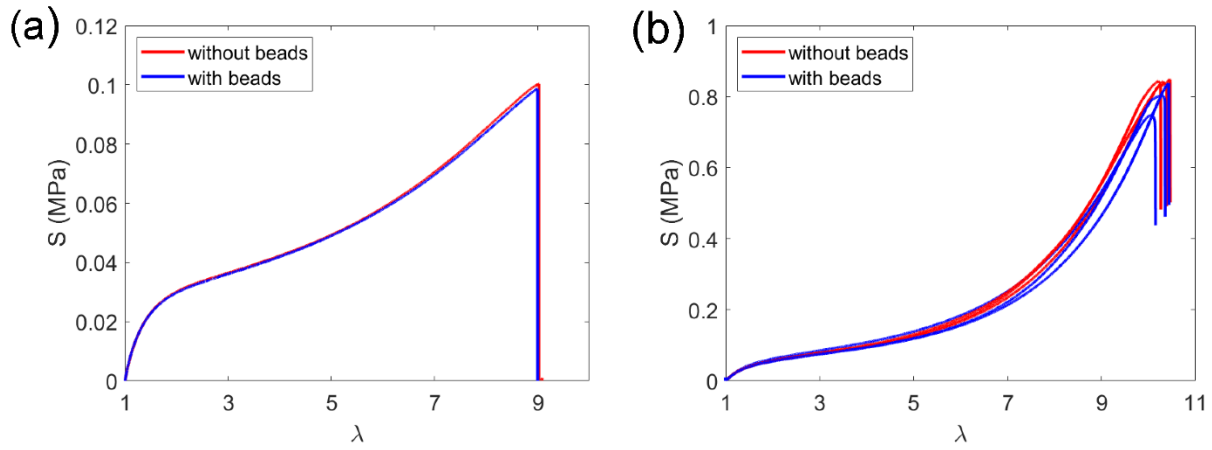

Figure 6. Effects of tracer beads on the mechanical property of the PA gel. Nominal stress S versus stretch ratio λ under uniaxial tension for PA gel samples with or without beads: **(a)** initial stretch rate $\dot{\lambda} = 10^{-3}$ s^{-1} using the sample with pure shear geometry (50 mm × 10 mm × 1.7 mm, $L_0 \times H_0 \times t_0$); **(b)** initial stretch rate $\dot{\lambda} = 0.2$ s^{-1} using the sample with dumbbell geometry (gauge length = 12 mm, width = 2 mm, thickness = 1.7 mm).

Appendix C. Images for the slow loading case

Figure 7 shows images of the PA gel sample and the tracer particles on the gel surface at 9 different times for the slow loading case (initial stretch rate $\dot{\lambda} = 10^{-3}$ s^{-1} and prescribed stretch $\lambda_{hold} = 3.8$). This experiment (from $t = 0$ s to 4340 s) was recorded with a rate of 1 frame per 5 seconds.

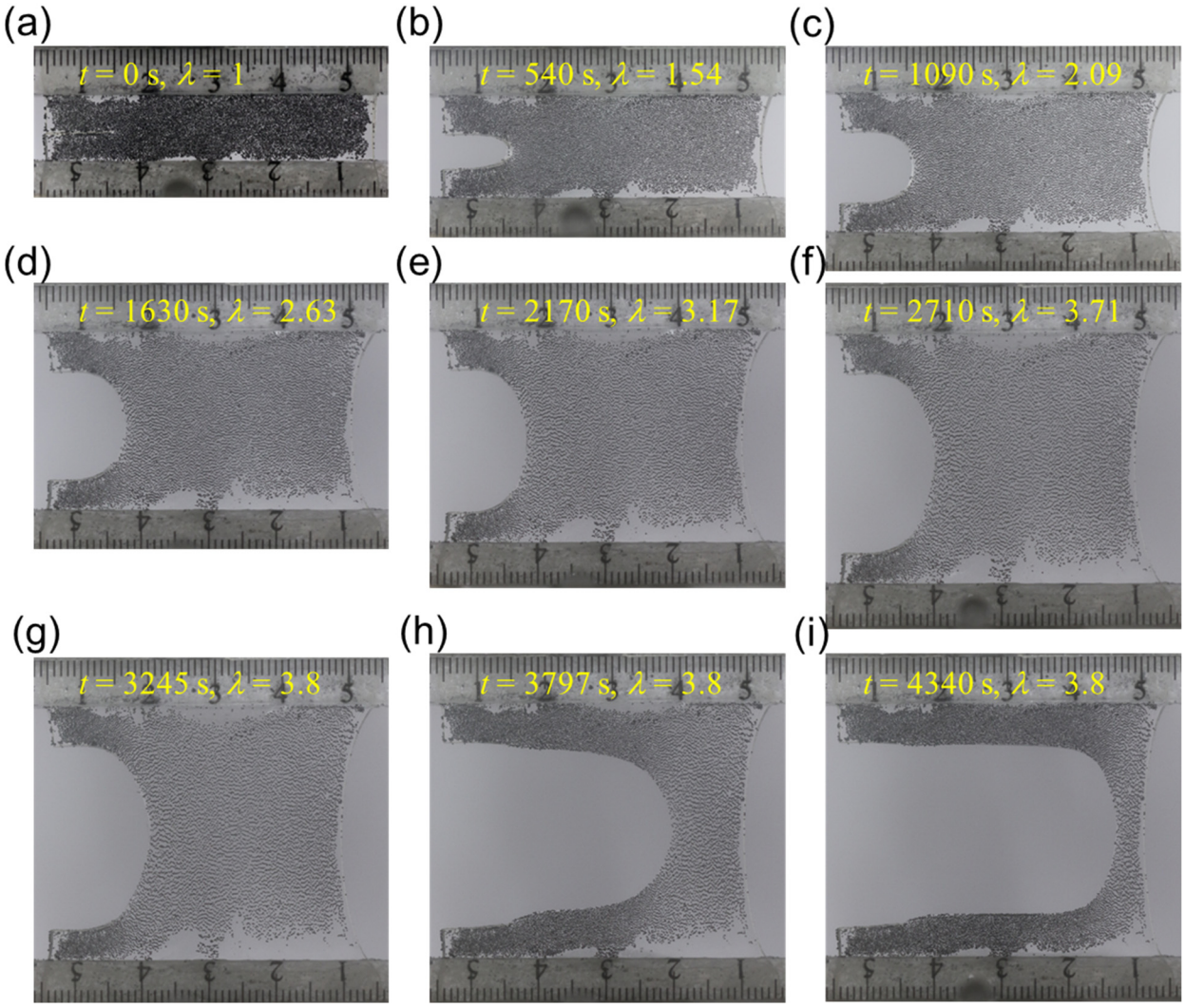

Figure 7. Images of the PA gel sample with tracer particles in the slow loading case ($\dot{\lambda} = 10^{-3}$ s^{-1} and $\lambda_{hold} = 3.8$) at different times throughout the experiment. The sample was first loading to $\lambda_{hold} = 3.8$ (corresponding to $t = 2800$ s), then the clamps was held fixed to track the crack propagation.

Appendix D. Two stages of crack propagation

For the fast loading case ($\dot{\lambda} = 0.05\ \text{s}^{-1}$ and $\lambda_{hold} = 3.8$), we measured the crack tip displacement c as schematically illustrated in see Fig. 1a, and plotted c versus time t in Fig.8a. The corresponding true crack extension C is plotted in Fig.8b. The time when crack propagation started can be determined from Fig.8b, but is not obvious in Fig.8a. Similar to the slow loading case ($\dot{\lambda} = 10^{-3}$ s^{-1} and $\lambda_{hold} = 3.8$), two stages of crack propagation and a sudden acceleration from Stage I to Stage II are observed. For Stage I, the crack tip velocity is $v_I = 1.33\times10^{-2}$ mm/s and the crack extension speed is $V_I = 1.42\times10^{-2}$ mm/s, which are determined using the slopes between $t = 104$ s and 270 s in Fig.8a and Fig.8b, respectively. For Stage II, the crack tip velocity is $v_{II} = 0.45$ mm/s and the crack extension speed is $V_{II} = 0.47$ mm/s, which are determined using the slopes between $t = 315$ s and 338 s in Fig.8a and Fig.8b, respectively. Note that the four time points at $t = 104$ s, 270 s, 315s and 338 s are marked as C1, C2, C3 and C4 on Fig.10a, respectively.

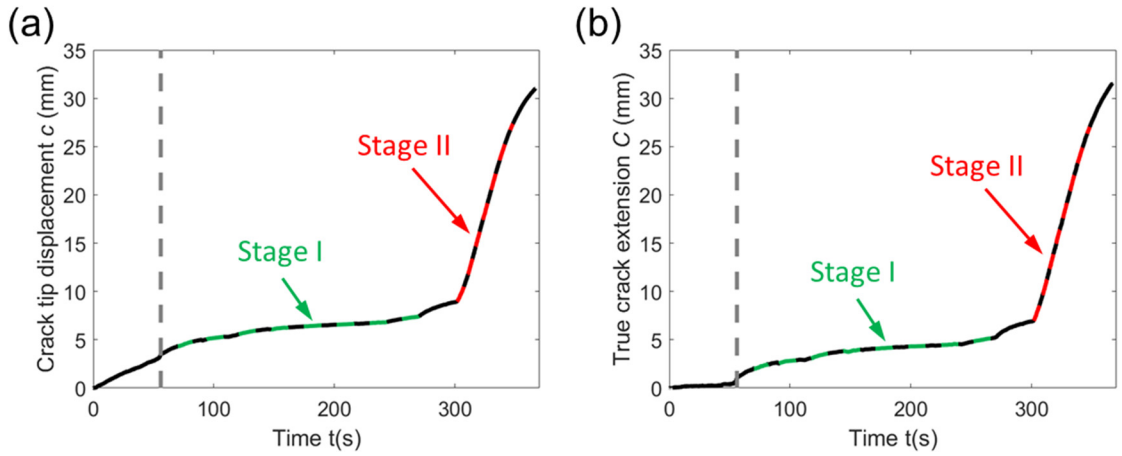

Figure 8. Crack propagation for the fast loading case ($\dot{\lambda} = 0.05\ \text{s}^{-1}$ and $\lambda_{hold} = 3.8$). **(a)** History of the crack tip displacement c measured in the deformed configuration. **(b)** History of the true crack extension C measured in the reference configuration. The vertical dashed line indicates the beginning of holding.

We repeated the crack propagation experiments using the same initial loading rate as the slow loading case ($\dot{\lambda} = 10^{-3}\ \text{s}^{-1}$) but different prescribed stretch λ_{hold} at holding. We consistently observed the two stages of crack propagation. The crack tip velocities v, defined as $v \equiv dc/dt$

where c is the crack tip displacement measured in the deformed configuration, for these two stages under different λ_{hold} are shown in Fig.9a. Furthermore, experiments under a much higher initial stretch rate ($\dot{\lambda} = 1\ s^{-1}$) and different prescribed stretch λ_{hold} also exhibited the two stages of crack propagation and the sudden acceleration between them (Fig.9b).

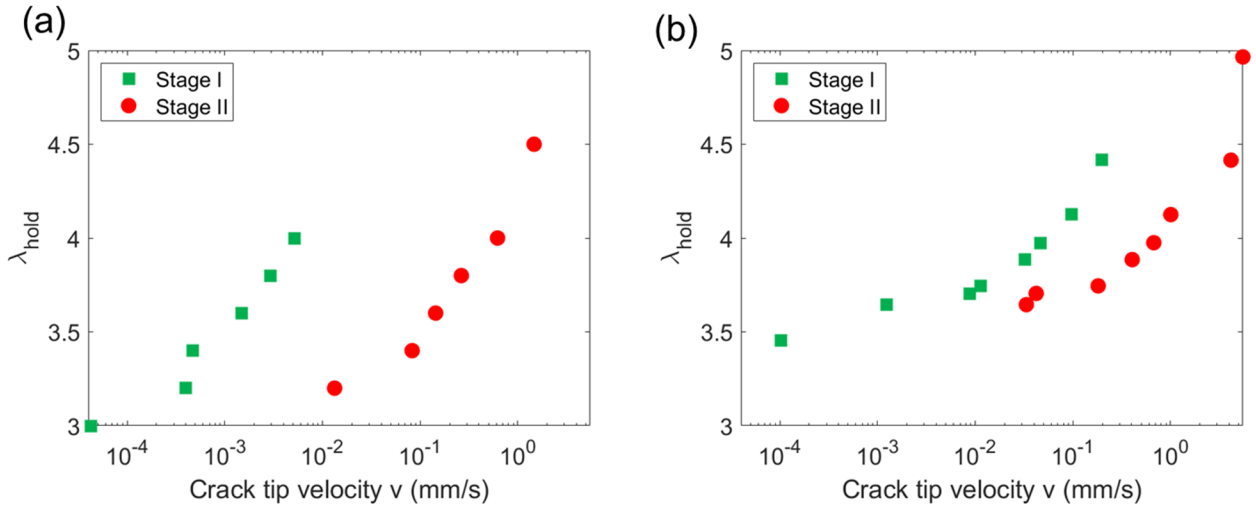

Figure 9. Two stages of crack propagation. Crack tip velocity v (measured in the deformed configuration) at different global stretch ratio λ_{hold}. **(a)** Data for the slow initial loading rate (initial stretch rate $\dot{\lambda} = 10^{-3}\ s^{-1}$). **(b)** Data for a much higher initial loading rate (initial stretch rate $\dot{\lambda} = 1\ s^{-1}$). Green squares and red circles represent data points in Stage I and II, respectively.

Appendix E. Deformation fields for the fast loading case

The fast loading case ($\dot{\lambda}$ = 0.05 s^{-1} and λ_{hold} = 3.8) was analyzed with the same procedures as the slow loading case (see Fig.2 and associated discussions), as shown in Fig.10 below.

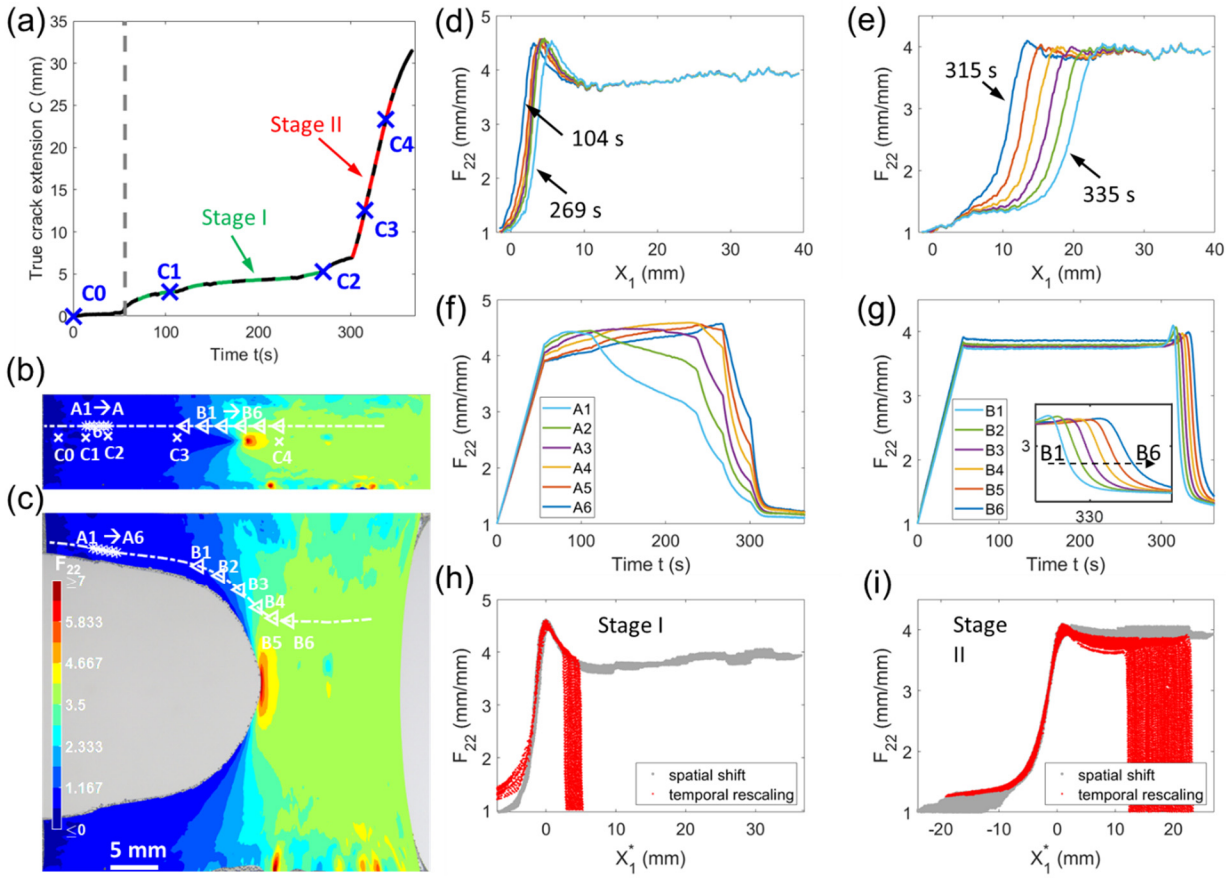

Figure 10. True crack extension and deformation field for the fast loading case ($\dot{\lambda}$ = 0.05 s^{-1} and λ_{hold} = 3.8). **(a)** True crack extension C versus time. The vertical dashed line indicates when holding started. **(b-c)** Distribution of F_{22} at t = 330.5 s plotted in **(b)** the initial configuration and **(c)** the deformed configuration. In **(b)** and **(c)** the same color bar and scale bar are used. The reference crack tip positions at C0 (t = 0 s), C1 (t = 104 s), C2 (t = 270 s), C3 (t = 315 s), and C4 (t = 338 s) are marked in **(b)**. The initial crack tip at C0 is located at $X_1 = X_2 = 0$, and C1-C4 occurred during holding ($\lambda = \lambda_{hold}$ = 3.8). **(d-e)** Spatial distributions of F_{22} along the horizontal line (X_2 = 1.22 mm) at different times during holding in **(d)** Stage I (t = 104 to 269 s with an equal increment of 33 s) and **(e)** Stage II (t = 315 to 335 s with an equal increment of 4 s). **(f-g)** Histories of F_{22} at **(f)** A1-A6 and **(g)** B1-B6 on the horizontal line of X_2 = 1.22 mm. **(h-i)** Data points of spatial shift (grey) and temporal rescaling (red) for F_{22} during **(h)** Stage I and **(i)** Stage II.

Appendix F. Constitutive model of PA gel: nonlinear viscoelasticity

We adopt a recently developed constitutive model (Venkata et al., 2021) to capture nonlinear viscoelastic behavior of polyampholyte (PA) gels with chemical and physical crosslinks. The physical picture and mathematical formulation of this model are briefly summarized in the following.

General formulation

The PA gel network is divided into a permanent network containing chains connected by the chemical crosslinks and a transient network containing temporary chains connected by physical crosslinks. If all chains were permanently connected, the gel network would be hyperelastic and be governed by a strain energy density function W. Specifically, the incompressible Yeoh model is adopted for W, which gives

$$W\left(I_1\right)=\sum_{i=1}^{3}\xi_i\left(I_1-3\right)^i, \tag{15}$$

where I_1 is the trace of the right Cauchy-Green tensor, i.e., I_1 = trace($\mathbf{F}^{\mathrm{T}}\mathbf{F}$), $\mathbf{F}$ is the deformation gradient tensor and ξ_i are material parameters (unit: kPa). However, the temporary chains connected by physical crosslinks are not always attached to the network. They undergo detachment and reattachment due to the breaking and reforming of physical crosslinks. This process dissipates the strain energy stored in the temporary chains and leads to macroscopic viscoelasticity. To model this effect, one needs to keep track of the detaching and reattaching events of temporary chains.

Let ω_{chem} and ω_{phys} denote the fraction of permanent chains and temporary chains, respectively. By definition $\omega_{chem} + \omega_{phys} = 1$. The connected temporary chains undergo detachment governed by the breaking kinetics of physical crosslinks. This effect is described by the survivability function $\phi_B(\tau, t)$, which is defined as the fraction of temporary chains that are born at time τ and survived until t ($t \geq \tau$). By assuming strain-dependent breaking kinetics and integrating it over time, the following form of the survivability function is established (Venkata et al., 2021):

$$\phi_B\left(\tau,t\right)=\left[1+\frac{\alpha_B-1}{t_B}\int_{\tau}^{t}f\left(H^{\tau\to\tau'}\right)d\tau'\right]^{\frac{1}{1-\alpha_B}}, \tag{16}$$

where α_B is a dimensionless parameter ($1 < \alpha_B < 2$), t_B is the characteristic time of breaking kinetics and f is a dimensionless function ($f \geq 1$) to capture the effect that strained chains tend to break faster. The argument of the f function, $H^{\tau\to\tau'}$, represents the deformation history experienced by the chains from time τ to time τ'. Specifically,

$$H^{\tau\to\tau'} = \text{trace}\left[\left(\mathbf{F}^{\tau\to\tau'}\right)^T\left(\mathbf{F}^{\tau\to\tau'}\right)\right], \tag{17}$$

where $\mathbf{F}^{\tau\to\tau'}$ is the deformation gradient tensor measured from time τ to time τ'. An underlying assumption of the function f is that newly formed temporary chains are in a relaxed configuration. Therefore, temporary chains born at time τ can only experience the deformation history after time τ. It is also assumed that one can use the trace of the deformation gradient $\mathbf{F}^{\tau\to\tau'}$ to represent the effect of strain on the breaking kinetics. Following the formulation in Venkata et al. (2021), the function f is given by

$$f\left(H^{\tau\to\tau'}\right) = \left(1 + \frac{H^{\tau\to\tau'} - 3}{I_c - 3}\right)^m, \tag{18}$$

where m and I_c are dimensionless parameters. In particular, I_c is the critical deformation at which the breaking kinetics of temporary chains starts to increase rapidly.

The reattachment rate of temporary chains is assumed to be proportional to the amount of broken temporary chains and independent of strain, since the broken temporary chains are relaxed. Let $\chi(t)$ be the fraction of newly reattached temporary chains per unit time at time t. It can be solved using the following equation (Venkata et al., 2021):

$$1 - \omega_{chem} = \chi(t)t_H + \int_{-\infty}^{t} \phi_B(\tau, t)\chi(\tau)d\tau, \tag{19}$$

where t_H is the characteristic time for chain reattachment. To understand Eq. (19), we note that $\chi(t)t_H$ is equal to the fraction of broken temporary chains at time t, while the integral is the fraction of connected temporary chains at time t. Therefore, the right hand side of Eq. (19) is equal to the total fraction of temporary chains ω_{phys}.

Based on the physical picture described above, the total strain energy density Ψ of the PA gel network at time t is given by

$$\Psi(t) = \omega_{chem} W\left(I_1(t)\right) + \int_{-\infty}^{t} \left[\chi(\tau)\phi_B(\tau,t) W\left(H^{\tau\to t}\right)\right] d\tau \,. \tag{20}$$

The first term on the right hand side of Eq. (20) is the contribution from the permanent chains. Without loss of generality, we can assume deformation starts at $t = 0$. The deformation from $t = 0$ to the current time t is $\mathbf{F}^{0\to t}$. Therefore, $I_1(t) = \text{trace}[(\mathbf{F}^{0\to t})^{\mathrm{T}} \mathbf{F}^{0\to t}]$. Based on the definition in Eq. (17), $I_1(t) \equiv H^{0\to t}$. The integral on the right hand side of Eq. (20) is motivated by the assumption that the temporary chains born at time τ only experience the deformation history from time τ to the current time t, which is represented by $H^{\tau\to t} \equiv \text{trace}[(\mathbf{F}^{\tau\to t})^{\mathrm{T}} \mathbf{F}^{\tau\to t}]$.

Constitutive equation for the stress can be derived using the Coleman-Noll procedure (Holzapfel, 2000), as shown in the supplementary material of Venkata et al. (2021). This procedure yields the following expression for the first Piola-Kirchhoff stress tensor **S**:

$$\mathbf{S}(t) = -p\left(\mathbf{F}^{0\to t}\right)^{-T} + \omega_{chem}\, 2\frac{dW}{dI_1}\bigg|_{I_1 = I_1(t)} \mathbf{F}^{0\to t} + \int_{-\infty}^{t} \chi(\tau)\phi_B(\tau,t)\, 2\frac{dW}{dI_1}\bigg|_{I_1 = H^{\tau\to t}} \mathbf{F}^{\tau\to t}\left(\mathbf{F}^{0\to\tau}\right)^{-T} d\tau \,, \tag{21}$$

where p is the Lagrange multiplier to enforce the incompressibility condition.

Kinetics before deformation

Both Eq. (20) and Eq. (21) involve time integrals for τ ranging from $-\infty$ to the current time t. Since deformation starts at $t = 0$, we divide the time interval into two: $\tau < 0$ and $0 \le \tau \le t$. For $\tau < 0$, since there is no deformation before $t = 0$, we have $H^{\tau\to t} = H^{0\to t} = I_1(t)$, $\mathbf{F}^{\tau\to t} = \mathbf{F}^{0\to t}$ and $\mathbf{F}^{0\to\tau}$ is equal to the identity tensor. Therefore, Eq. (20) can be rewritten as

$$\Psi(t) = \left(\omega_{chem} + \int_{-\infty}^{0} \left[\chi(\tau)\phi_B(\tau,t)\right] d\tau\right) W(I_1) + \int_{0}^{t} \left[\chi(\tau)\phi_B(\tau,t) W\left(H^{\tau\to t}\right)\right] d\tau \,. \tag{22}$$

Before $t = 0$, we assume the detachment and reattachment of temporary chains are in a dynamic equilibrium with a constant reattachment rate χ^{ss}, which can be solved from Eq. (19). Note that the f function in $\phi_B(\tau, t)$ is equal to 1 for $t < 0$. The solution of χ^{ss} is

$$\chi^{ss} = \frac{1 - \omega_{chem}}{t_H + \dfrac{t_B}{2 - \alpha_B}} \,. \tag{23}$$

Furthermore,

$$\begin{aligned}\int_{-\infty}^{0}\phi_B(\tau,t)\,d\tau &= \int_{-\infty}^{0}\left[1+\frac{\alpha_B-1}{t_B}\int_{\tau}^{0}f\left(H^{\tau\to\tau'}\right)d\tau'+\frac{\alpha_B-1}{t_B}\int_{0}^{t}f\left(H^{0\to\tau'}\right)d\tau'\right]^{\frac{1}{1-\alpha_B}}d\tau \\ &= \int_{-\infty}^{0}\left[1-\frac{\alpha_B-1}{t_B}\tau+\frac{\alpha_B-1}{t_B}\int_{0}^{t}f\left(H^{0\to\tau'}\right)d\tau'\right]^{\frac{1}{1-\alpha_B}}d\tau=\frac{t_B}{2-\alpha_B}\left[1+\frac{\alpha_B-1}{t_B}\int_{0}^{t}f\left(H^{0\to\tau'}\right)d\tau'\right]^{\frac{2-\alpha_B}{1-\alpha_B}}\end{aligned}. \tag{24}$$

Therefore, we have

$$\int_{-\infty}^{0}\left[\chi(\tau)\phi_B(\tau,t)\right]d\tau=\chi^{ss}\frac{t_B}{2-\alpha_B}\left[1+\frac{\alpha_B-1}{t_B}\int_{0}^{t}f\left(H^{0\to\tau'}\right)d\tau'\right]^{\frac{2-\alpha_B}{1-\alpha_B}}=\frac{\chi^{ss}t_B}{2-\alpha_B}\left[\phi_B(0,t)\right]^{2-\alpha_B}. \tag{25}$$

Substituting Eq. (25) into Eq. (22), we obtain

$$\Psi(t)=\left(\omega_{chem}+\chi^{ss}\frac{t_B}{2-\alpha_B}\left[\phi_B(0,t)\right]^{2-\alpha_B}\right)W(I_1)+\int_{0}^{t}\left[\chi(\tau)\phi_B(\tau,t)W\left(H^{\tau\to t}\right)\right]d\tau. \tag{26}$$

Similarly, the first Piola-Kirchhoff stress tensor **S** in Eq. (21) becomes

$$\begin{aligned}\mathbf{S}(t) &= -p\left(\mathbf{F}^{0\to t}\right)^{-T}+\left(\omega_{chem}+\chi^{ss}\frac{t_B}{2-\alpha_B}\left[\phi_B(0,t)\right]^{2-\alpha_B}\right)2\left.\frac{dW}{dI_1}\right|_{I_1=I_1(t)}\mathbf{F}^{0\to t} \\ &+\int_{0}^{t}\chi(\tau)\phi_B(\tau,t)2\left.\frac{dW}{dI_1}\right|_{I_1=H^{\tau\to t}}\mathbf{F}^{\tau\to t}\left(\mathbf{F}^{0\to\tau}\right)^{-T}d\tau\end{aligned}. \tag{27}$$

Our experimental data based on particle tracking provide the history of the in-plane components of **F**, namely F_{11}, F_{12}, F_{21} and F_{22}. Assuming plane stress condition, the out-of-plane components $F_{31} = F_{32} = 0$, and F_{33} can be determined using the incompressibility condition det(**F**) = 1, which yields $F_{33} = 1/(F_{11}F_{22} - F_{12}F_{21})$. The Lagrange multiplier p in Eq. (27) was solved by using the plane stress condition $S_{33} = 0$. Therefore, we can use Eq. (27) to calculate all in-plane components of **S** using the data of **F** obtained from particle tracking. However, implementation of Eq. (27) is numerically expensive due to the multiple time integrals involved, i.e., the integral in Eq. (27), the function $\phi_B(\tau, t)$ in Eq. (16), and the reattachment rate $\chi(\tau)$ which needs to be solved using Eq. (19). To reduce the numerical cost, we follow the practice in Venkata et al. (2021) and replaced $\chi(\tau)$ in the integral of Eq. (27) by the constant χ^{ss}. We verified that this simplification

made negligible difference in the stress result, and it allowed us to avoid solving the integral equation in Eq. (19).

Parameter calibration

The constitutive model summarized above has been shown to provide good agreement with uniaxial tensile test data of PA gels under various loading histories and strain range. There are 9 independent parameters in this model, as listed in Table 2. Since the PA gel adopted in this work has a lower crosslinking density than that in Venkata et al. (2021), we performed cyclic tensile tests to calibrate these parameters.

Table 2. Parameters for the viscoelastic constitutive model.

Parameters	Meaning	Calibrated value
ω_{chem}	Fraction of the permanent chains	0.0458
α_B	Exponent in the survivability function Eq. (16)	1.8717
t_B	Characteristic time for breaking kinetics in Eq. (16)	0.05 s
t_H	Characteristic time for reforming kinetics in Eq. (19)	0.6865 s
m	Exponent in the strain-dependent function in Eq. (18)	3.3138
I_c	Critical deformation for strain dependent kinetics; Eq. (18)	8.7427
ξ_1	Parameter of the Yeoh model in Eq. (15)	52.82 kPa
ξ_2/ξ_1	Parameter of the Yeoh model in Eq. (15)	9.6517×10^{-4}
ξ_3/ξ_1	Parameter of the Yeoh model in Eq. (15)	3.3477×10^{-5}

Assuming the uniaxial tension is along the X_2 direction, we set $\lambda_1 = \lambda_3 = [\lambda_2(t)]^{-1/2}$, which means the deformation gradient tensor $\mathbf{F}$ is:

$$\mathbf{F}^{0\to t} = \left[\lambda_2(t)\right]^{-1/2}\left(\mathbf{e}_1 \otimes \mathbf{e}_1\right) + \lambda_2(t)\left(\mathbf{e}_2 \otimes \mathbf{e}_2\right) + \left[\lambda_2(t)\right]^{-1/2}\left(\mathbf{e}_3 \otimes \mathbf{e}_3\right), \tag{28}$$

where $\mathbf{e}_i$ (i = 1, 2, 3) are the unit vectors along X_1, X_2 and X_3 axes, respectively. Plugging Eq. (28) into the constitutive model and applying the boundary condition that $S_{11} = S_{33} = 0$, we obtain the following equation for the nominal tensile stress $S_{22}(t)$:

$$S_{22}(t)=2\left(\omega_{chem}+\chi^{ss}\frac{t_B}{2-\alpha_B}\left[\phi_B(0,t)\right]^{2-\alpha_B}\right)\left.\frac{dW}{dI_1}\right|_{I_1=I_1(t)}\left(\lambda_2(t)-\left[\lambda_2(t)\right]^{-2}\right)$$
$$+\int_0^t\chi(\tau)\phi_B(\tau,t)2\left.\frac{dW}{dI_1}\right|_{I_1=H^{\tau\to t}}\left[\frac{\lambda_2(t)}{\lambda_2^2(\tau)}-\frac{\lambda_2(\tau)}{\lambda_2^2(t)}\right]d\tau \quad , \qquad (29)$$

where

$$I_1(t)=\lambda_2^2(t)+2\lambda_2^{-1}(t) \quad \text{and} \quad H^{\tau\to t}=\lambda_2^2(t)\lambda_2^{-2}(\tau)+2\lambda_2^{-1}(t)\lambda_2(\tau). \qquad (30)$$

We fit Eq. (29) to a series of uniaxial tensile data with cyclic loading following the optimization procedures described in the supplementary material of Venkata et al. (2021). The tensile data features two different strain rate (0.042 s^{-1} and 0.083 s^{-1}) and 9 different peak stretch (ranging from 2 to 10). As shown in Fig.11 and Fig.12, the constitutive model can well capture the experimental data using the set of parameter values given in Table 2. The data in Fig.11a-11h are the same as those in Fig.3a of the main text except that they are separated into different subplots to facilitate comparison between the model fits and experimental data.

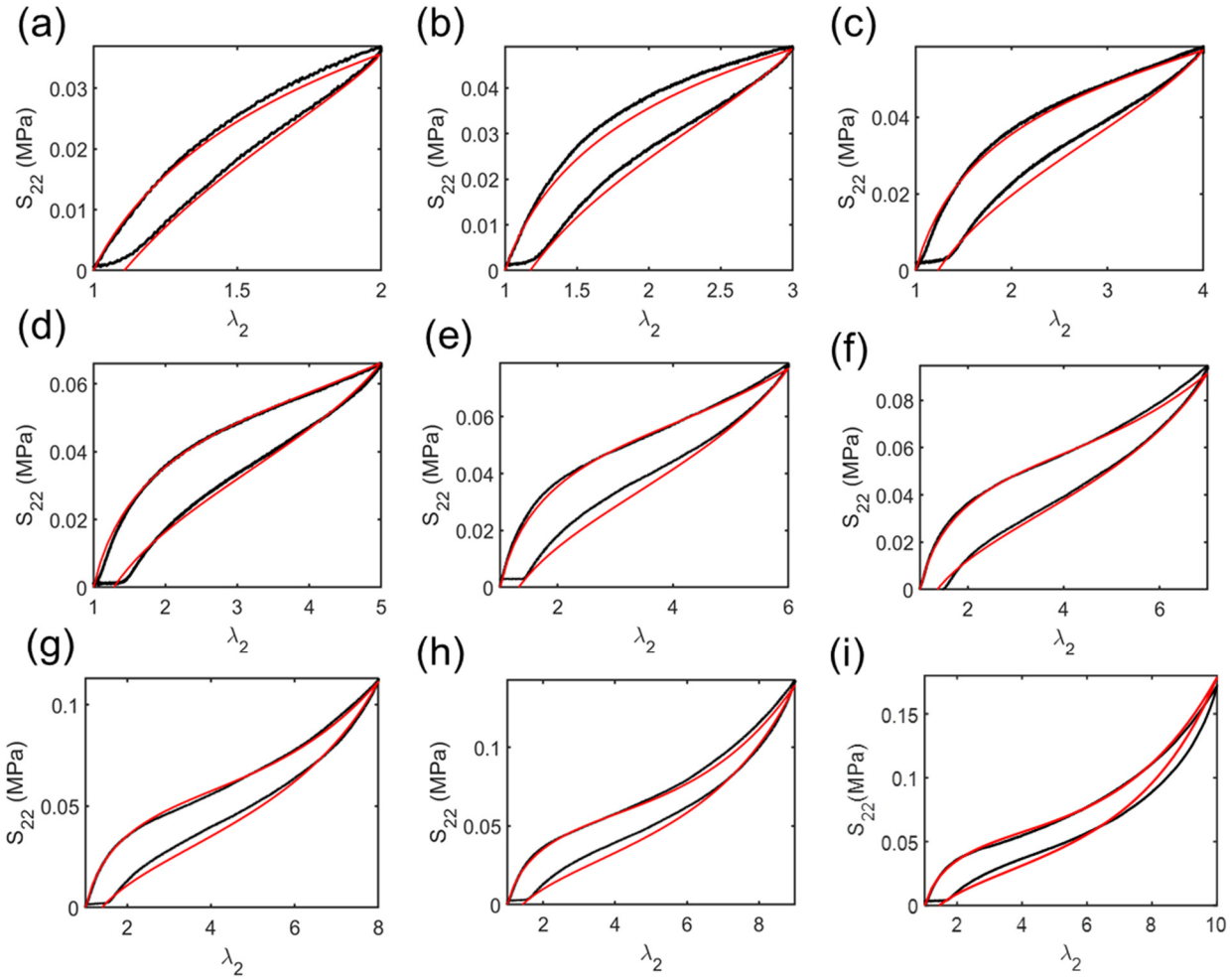

Figure 11. Calibration of the constitutive model using uniaxial tension data. Nominal stress S_{22} versus stretch ratio λ_2 under cyclic loading with constant strain rate 0.042 s^{-1} for both loading and unloading. In **(a-i)**, each subplot represents an independent cyclic test with different peak stretch (ranging from 2 to 10). In all subplots the black line represents experimental data and the red line represents model fit.

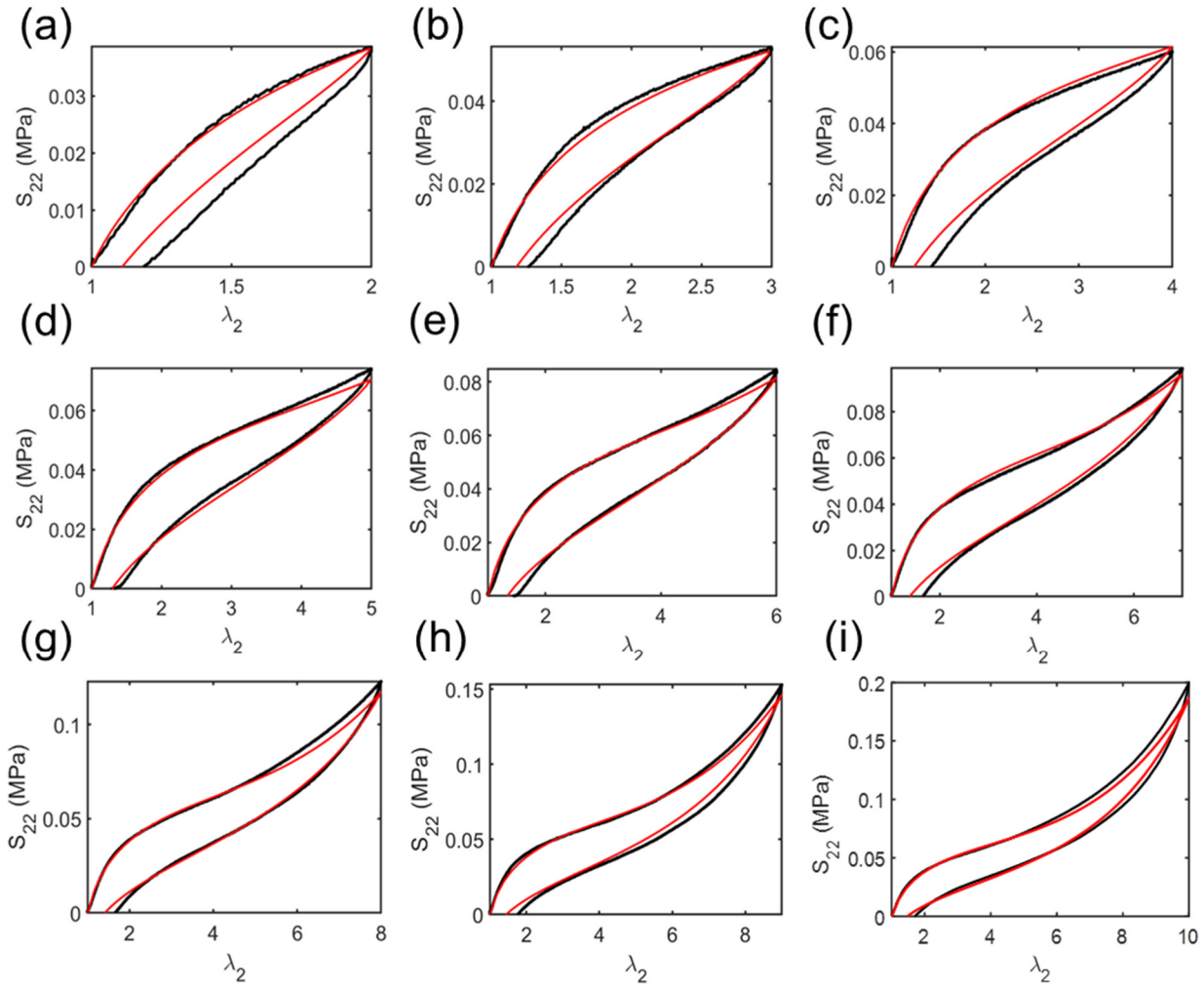

Figure 12. Calibration of the constitutive model using uniaxial tension data. Nominal stress S_{22} versus stretch ratio λ_2 under cyclic loading with constant strain rate 0.083 s^{-1} for both loading and unloading. In **(a-i)**, each subplot represents an independent cyclic test with different peak stretch (ranging from 2 to 10). In all subplots the black line represents experimental data and the red line represents model fit.

Appendix G. Supplementary movies

Movie S1.

Deformation fields in the slow loading case ($\dot{\lambda}$ = 10^{-3} s^{-1} and λ_{hold} = 3.8). Contours of the deformation gradient components F_{11} (top left), F_{12} (top right), F_{21} (bottom left) and F_{22} (bottom right) shown in the deformed configurations. The time is accelerated by 150 times.

Movie S2.

Deformation fields in the slow loading case ($\dot{\lambda}$ = 0.05 s^{-1} and λ_{hold} = 3.8). Contours of the deformation gradient components F_{11} (top left), F_{12} (top right), F_{21} (bottom left) and F_{22} (bottom right) shown in the deformed configurations. The time is accelerated by 3 times.

Movie S3.

Time evolution of the deformation and dissipation fields in the slow loading case ($\dot{\lambda}$ = 10^{-3} s^{-1} and λ_{hold} = 3.8). Contours of the deformation gradient component F_{22} (top left), the deformation gradient rate $\dot{F}_{22}$ (top right), the accumulated dissipation density $\int_0^t D dt$ (bottom left), and the dissipation power density D (bottom right) shown in the initial configuration. The time is accelerated by 150 times.

Movie S4.

Time evolution of the deformation and dissipation fields in the fast loading case ($\dot{\lambda}$ = 0.05 s^{-1} and λ_{hold} = 3.8). Contours of the deformation gradient component F_{22} (top left), the deformation gradient rate $\dot{F}_{22}$ (top right), the accumulated dissipation density $\int_0^t D dt$ (bottom left), and the dissipation power density D (bottom right) shown in the initial configuration. The time is accelerated by 3 times.

Appendix H. Integration region for stress work, dissipation and free energy

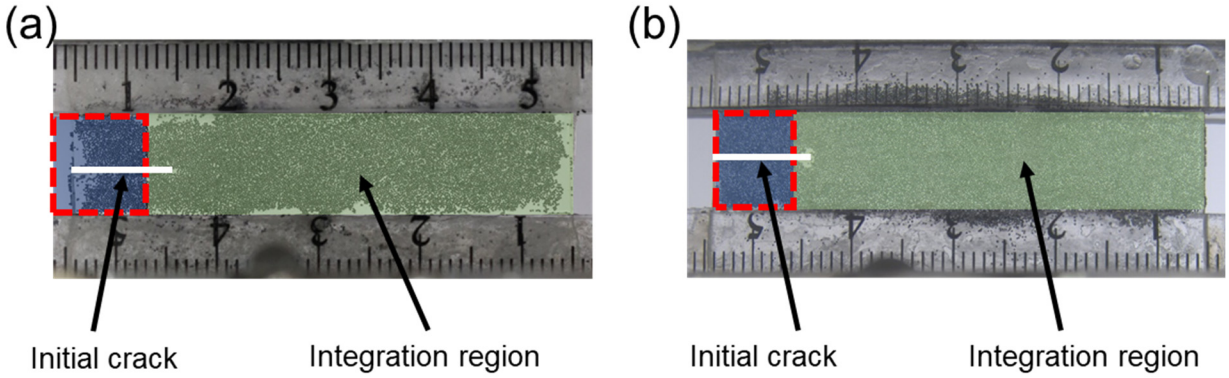

Figure 13. Illustrations of the region used to perform integration for U_S, U_D and U_E. **(a)** Slow loading case ($\dot{\lambda}$ = 10^{-3} s^{-1} and λ_{hold} = 3.8). **(b)** Fast loading case ($\dot{\lambda}$ = 0.05 s^{-1} and λ_{hold} = 3.8). The white line represents the initial crack and the region shaded in light green is the tracked region used for integration. The region behind the initial crack tip (i.e., boxed by red dashed lines) was removed from the integration since this area did not undergo any deformation.

Appendix I. Fracture toughness of crack growth initiation

Procedures for measuring the fracture toughness of crack growth initiation, Γ^{init}, are shown in Fig.14. Briefly, we prepared unnotched and notched PA gel samples with the same dimensions as the samples described in Section 2.2 (i.e., L_0 = 50 mm, H_0 = 10 mm and thickness = 1.7 mm). For notched samples, a 10-mm pre-notch was introduced to the sample (Fig.14a). The notched samples were subjected to continuous stretch at a constant loading rate $\dot{\lambda}$ to determine the critical stretch ratio λ_c at the onset of crack growth (Fig.14b and 14c). Because of the rate-dependence of the PA gel, we applied the same loading rate as the crack propagation experiments, i.e., $\dot{\lambda}$ = 0.05 s^{-1} (Fig.14b) or 10^{-3} s^{-1} (Fig.15a). The critical stretch λ_c exhibited a dependence on the loading rate (Table 3), i.e., λ_c decreased as $\dot{\lambda}$ was increased. The unnotched samples were used to determine the strain energy density stored in materials points far ahead of the crack tip (Fig.14d). We first stretched the unnotched sample at a constant loading rate $\dot{\lambda}$ = 0.05 s^{-1} (Fig.14e) or 10^{-3} s^{-1} (Fig.15b) until $\lambda = \lambda_c$ and then unloaded it at different rates.

The area underneath the loading branch (Fig.14f), denoted as W_{load}, represents the mechanical work done to a unit volume of the sample material. For elastic materials, W_{load} is fully stored in the material and is released for driving crack growth in the corresponding notched sample. This is quantified by the energy release rate G. For the pure shear geometry, $G = W_{\text{load}} H_0$. By evaluating W_{load} at the critical stretch λ_c, one can obtain the critical energy release rate $G_c = W_{\text{load}}(\lambda_c) H_0$, which is taken as the fracture toughness Γ^{init} for initiating crack growth.

The calculation above is based on the assumption of elasticity. However, PA gel is viscoelastic and can dissipate energy under loading. As a result, the energy release rate G for the initiation of crack growth may not be well defined (Long and Hui, 2016). Here we adopt an approximation in the literature (Mayumi et al., 2016; Zhang et al., 2022) that uses the area underneath unloading branch, W_{unload}, to determine Γ^{init}. Physically W_{unload} represents the strain energy per unit volume released during unloading of the unnotched sample. It provides a better estimate for the strain energy available for driving crack growth in the notched sample. Therefore, we calculate Γ^{init} using $\Gamma^{\text{init}} = W_{\text{unload}}(\lambda_c) H_0$. A further complication is that the unloading branch, and hence W_{unload},

is dependent on the unloading rate (Fig.14e and Fig.15b). Therefore, we calculated the W_{unload} for two different unloading rates and list the resulting Γ^{init} in Table 3. It is of interest to compare Γ^{init} and the Γ_0 obtained using our full field approach because Γ^{init} is often reported in the literature and, unlike Γ_0, the measurement of Γ^{init} is independent of the constitutive model of the PA gel.

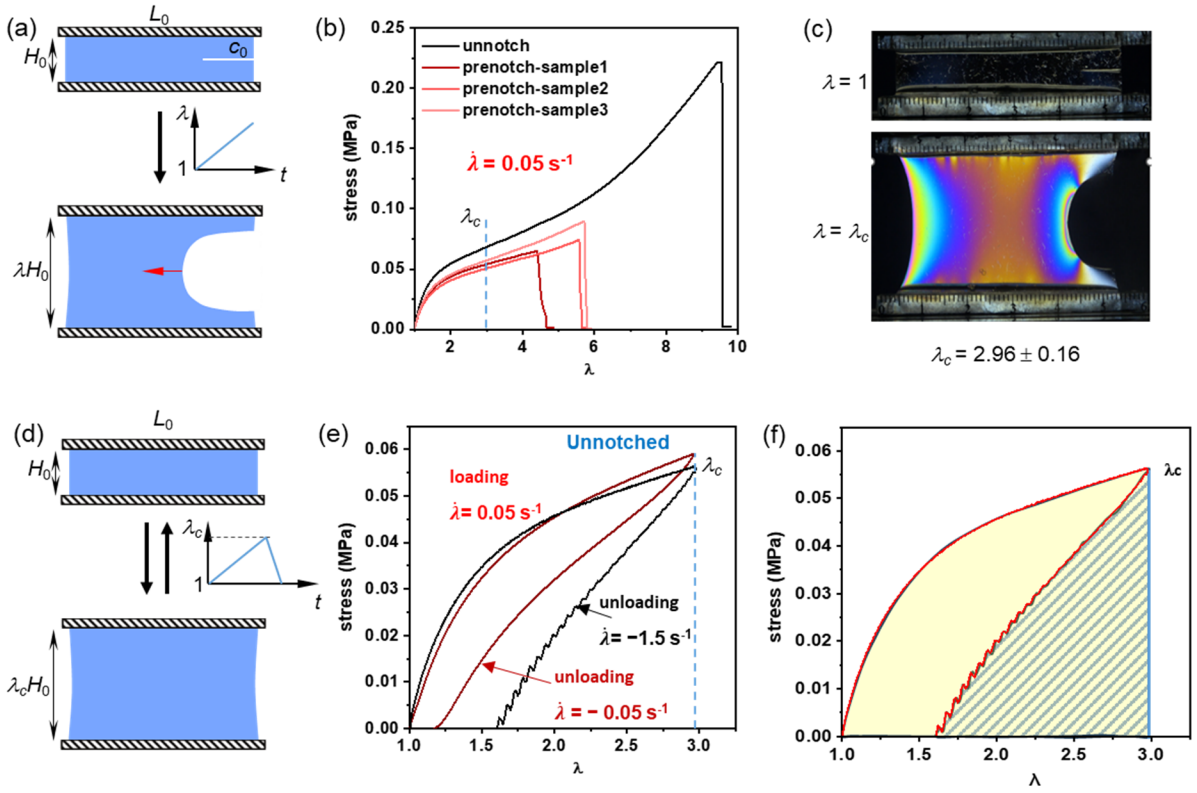

Figure 14. Measuring the fracture toughness at crack growth initiation. **(a)** Pure shear test used to measure Γ^{init}. **(b)** Effective nominal stress versus stretch curves for the pure shear test at a loading rate of $\dot{\lambda} = 0.05\ \text{s}^{-1}$. **(c)** Birefringence images of an undeformed sample and a sample loaded to the critical stretch ratio λ_c for initiating crack growth. **(d)** Experimental protocol for determining the stored strain energy at the critical stretch. **(e)** Nominal stress versus stretch curves for an unnotched sample loaded to λ_c at $\dot{\lambda} = 0.05\ \text{s}^{-1}$ and subsequently unloaded at two different rates. **(f)** The area underneath the loading curve (highlighted in light yellow) is denoted as W_{load}, and the area underneath the unloading curve (highlighted in hatch lines) is denoted as W_{unload}.

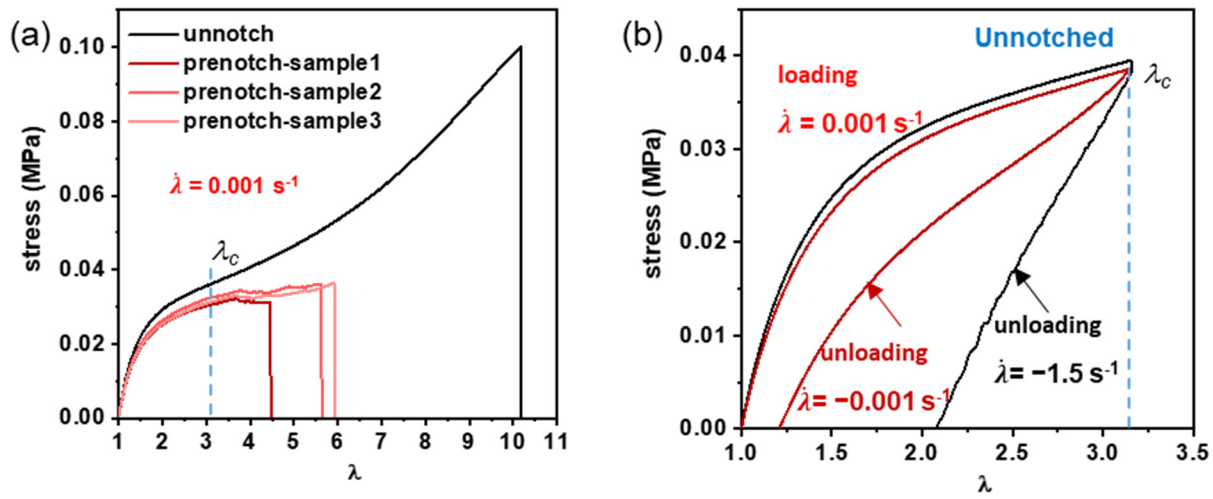

Figure 15. Fracture toughness of crack growth initiation for loading rate $\dot{\lambda} = 10^{-3}$ s^{-1}. **(a)** Effective nominal stress versus stretch curves for the pure shear test. The critical stretch ratio λ_c for initiating crack growth is 3.16 ± 0.04. **(b)** Nominal stress versus stretch curves for an unnotched sample loaded to λ_c and subsequently unloaded at two different rates.

Table 3. Fracture energy for initiating crack growth in PA gel.

Loading rate (s^{-1})	λ_c	Γ^{init} (J/m^2)^a	Γ^{init} (J/m^2)^b
10^{-3}	3.16 ± 0.04	435	233
0.05	2.96 ± 0.16	566	404

^{a} Calculated from unloading curve with unloading rate = loading rate. ^{b} Calculated from unloading curve with unloading rate = 1.5 s^{-1}.

References

Bai, R., Yang, J., Suo, Z., 2019. Fatigue of hydrogels. Eur. J. Mech. A/Solids 74, 337–370. https://doi.org/10.1016/j.euromechsol.2018.12.001

Bonn, D., Kellay, H., Prochnow, M., Ben-Djemiaa, K., Meunier, J., 1998. Delayed fracture of an inhomogeneous soft solid. Science 280, 265–267. https://doi.org/10.1126/SCIENCE.280.5361.265/ASSET/BBAE176F-B48A-4E5D-A926-A3CF060B9536/ASSETS/GRAPHIC/SE1386389005.JPEG

Ciavarella, M., Cricri, G., McMeeking, R., 2021. A comparison of crack propagation theories in viscoelastic materials. Theor. Appl. Fract. Mech. 116, 103113. https://doi.org/10.1016/j.tafmec.2021.103113

Creton, C., 2003. Pressure-sensitive adhesives: An introductory course. MRS Bull. 28, 434–439. https://doi.org/10.1557/mrs2003.124

Creton, C., Ciccotti, M., 2016. Fracture and adhesion of soft materials: a review. Reports Prog. Phys. 79, 046601. https://doi.org/10.1088/0034-4885/79/4/046601

de Gennes, P.G., 1996. Soft adhesives. Langmuir 12, 4497–4500. https://doi.org/10.1021/la950886y

Feng, X., Hall, M.S., Wu, M., Hui, C.Y., 2014. An adaptive algorithm for tracking 3D bead displacements: Application in biological experiments. Meas. Sci. Technol. 25, 55701. https://doi.org/10.1088/0957-0233/25/5/055701

Gent, A.N., 1996. Adhesion and strength of viscoelastic solids. Is there a relationship between adhesion and bulk properties? Langmuir 12, 4492–4495. https://doi.org/10.1021/la950887q

Gent, A.N., Lai, S.-M., 1994. Interfacial bonding, energy dissipation, and adhesion. J. Polym. Sci. Part B Polym. Phys. 32, 1543–1555. https://doi.org/10.1002/polb.1994.090320826

Graham, G.A.C., 1968. The correspondence principle of linear viscoelasticity theory for mixed boundary value problems involving time-dependent boundary regions. Q. Appl. Math. 26, 167–174. https://doi.org/10.1090/qam/99860

Greensmith, H.W., 1964. Rupture of rubber. XI. Tensile rupture and crack growth in a noncrystallizing rubber. J. Appl. Polym. Sci. 8, 1113–1128. https://doi.org/10.1002/app.1964.070080308

Greenwood, J.A., 2004. The theory of viscoelastic crack propagation and healing. J. Phys. D. Appl. Phys. 37, 2557–2569. https://doi.org/10.1088/0022-3727/37/18/011

Guo, J., Long, R., Mayumi, K., Hui, C.Y., 2016. Mechanics of a dual cross-Link gel with dynamic bonds: Steady state kinetics and large deformation effects. Macromolecules 49, 3497–3507. https://doi.org/10.1021/acs.macromol.6b00421

Guo, J., Zehnder, A.T., Creton, C., Hui, C.Y., 2020. Time dependent fracture of soft materials: Linear: versus nonlinear viscoelasticity. Soft Matter 16, 6163–6179. https://doi.org/10.1039/d0sm00097c

Guo, Q., Caillard, J., Colombo, D., Long, R., 2022. Dynamic effect in the fatigue fracture of viscoelastic solids. Extrem. Mech. Lett. 54, 101726. https://doi.org/10.1016/j.eml.2022.101726

Hall, M.S., Long, R., Hui, C.Y., Wu, M., 2012. Mapping three-dimensional stress and strain fields within a soft hydrogel using a fluorescence microscope. Biophys. J. 102, 2241–2250. https://doi.org/10.1016/j.bpj.2012.04.014

Holzapfel, G.A., 2000. Nonlinear solid mechanics : a continuum approach for engineering. Wiley.

Hui, C.Y., Xu, D. Ben, Kramer, E.J., 1992. A fracture model for a weak interface in a viscoelastic material (small scale yielding analysis). J. Appl. Phys. 72, 3294–3304. https://doi.org/10.1063/1.351451

Hui, C.Y., Zhu, B., Long, R., 2022. Steady state crack growth in viscoelastic solids: A comparative study. J. Mech. Phys. Solids 159, 104748. https://doi.org/10.1016/j.jmps.2021.104748

Humphrey, J.D., 2003. Continuum biomechanics of soft biological tissues. Proc. R. Soc. A Math. Phys. Eng. Sci. https://doi.org/10.1098/rspa.2002.1060

Ihsan, A. Bin, Sun, T.L., Kurokawa, T., Karobi, S.N., Nakajima, T., Nonoyama, T., Roy, C.K., Luo, F., Gong, J.P., 2016. Self-healing behaviors of tough polyampholyte hydrogels. Macromolecules 49, 4245–4252. https://doi.org/10.1021/acs.macromol.6b00437

Karobi, S.N., Sun, T.L., Kurokawa, T., Luo, F., Nakajima, T., Nonoyama, T., Gong, J.P., 2016. Creep Behavior and Delayed Fracture of Tough Polyampholyte Hydrogels by Tensile Test. Macromolecules 49, 5630–5636. https://doi.org/10.1021/ACS.MACROMOL.6B01016/ASSET/IMAGES/MA-2016-010168_M001.GIF

Kim, J., Zhang, G., Shi, M., Suo, Z., 2021. Fracture, fatigue, and friction of polymers in which entanglements greatly outnumber cross-links. Science 374, 212–216. https://doi.org/10.1126/science.abg6320

Knauss, W.G., 2015. A review of fracture in viscoelastic materials. Int. J. Fract. 196, 99–146. https://doi.org/10.1007/s10704-015-0058-6

Knauss, W.G., 1973. On the steady propagation of a crack in a viscoelastic sheet: experiments and analysis, in: Kausch, H.H., Hassell, J.A., Jaffee, R.I. (Eds.), Deformation and Fracture of High Polymers. Springer US, pp. 501–541. https://doi.org/10.1007/978-1-4757-1263-6_27

Lake, G.J., Lindley, P.B., 1964. Cut growth and fatigue of rubbers. II. Experiments on a noncrystallizing rubber. J. Appl. Polym. Sci. 8, 707–721. https://doi.org/10.1002/app.1964.070080212

Lake, G.J., Thomas, A.G., 1967. The strength of highly elastic materials. Proc. R. Soc. London. Ser. A. Math. Phys. Sci. 300, 108–119. https://doi.org/10.1098/rspa.1967.0160

Li, X., Luo, F., Sun, T.L., Cui, K., Watanabe, R., Nakajima, T., Gong, J.P., 2023. Effect of Salt on Dynamic Mechanical Behaviors of Polyampholyte Hydrogels. Macromolecules 56, 535–544. https://doi.org/10.1021/acs.macromol.2c02003

Liu, W., Long, R., 2016. Constructing continuous strain and stress fields from spatially discrete displacement data in soft materials. J. Appl. Mech. Trans. ASME 83, 011006.

https://doi.org/10.1115/1.4031763

Long, R., Hui, C.Y., 2016. Fracture toughness of hydrogels: Measurement and interpretation. Soft Matter. https://doi.org/10.1039/c6sm01694d

Long, R., Hui, C.Y., 2015. Crack tip fields in soft elastic solids subjected to large quasi-static deformation - A review. Extrem. Mech. Lett. 4, 131–155. https://doi.org/10.1016/j.eml.2015.06.002

Long, R., Mayumi, K., Creton, C., Narita, T., Hui, C.Y., 2014. Time dependent behavior of a dual cross-link self-healing gel: Theory and experiments. Macromolecules 47, 7243–7250. https://doi.org/10.1021/ma501290h

Lu, Y., Qi, Y., Tenardi, M., Long, R., 2021. Mixed-mode fracture in a soft elastomer. Extrem. Mech. Lett. 48, 101380. https://doi.org/10.1016/j.eml.2021.101380

Luo, F., Sun, T.L., Nakajima, T., Kurokawa, T., Zhao, Y., Ihsan, A. Bin, Guo, H.L., Li, X.F., Gong, J.P., 2014. Crack blunting and advancing behaviors of tough and self-healing polyampholyte hydrogel. Macromolecules 47, 6037–6046. https://doi.org/10.1021/ma5009447

Mayumi, K., Guo, J., Narita, T., Hui, C.Y., Creton, C., 2016. Fracture of dual crosslink gels with permanent and transient crosslinks. Extrem. Mech. Lett. 6, 52–59. https://doi.org/10.1016/j.eml.2015.12.002

Morishita, Y., Tsunoda, K., Urayama, K., 2016. Velocity transition in the crack growth dynamics of filled elastomers: Contributions of nonlinear viscoelasticity. Phys. Rev. E 93, 043001. https://doi.org/10.1103/PhysRevE.93.043001

Persson, B.N.J., 2021. On opening crack propagation in viscoelastic solids. Tribol. Lett. 69, 1–8. https://doi.org/10.1007/s11249-021-01494-y

Persson, B.N.J., Brener, E.A., 2005. Crack propagation in viscoelastic solids. Phys. Rev. E 71, 036123. https://doi.org/10.1103/PhysRevE.71.036123

Qi, Y., Caillard, J., Long, R., 2018. Fracture toughness of soft materials with rate-independent hysteresis. J. Mech. Phys. Solids 118, 341–364. https://doi.org/10.1016/j.jmps.2018.05.020

Qi, Y., Zou, Z., Xiao, J., Long, R., 2019. Mapping the nonlinear crack tip deformation field in soft elastomer with a particle tracking method. J. Mech. Phys. Solids 125, 326–346. https://doi.org/10.1016/j.jmps.2018.12.018

Saulnier, F., Ondarçuhu, T., Aradian, A., Raphaël, E., 2004. Adhesion between a viscoelastic material and a solid surface. Macromolecules 37, 1067–1075. https://doi.org/10.1021/ma021759t

Schapery, R.A., 1975a. A theory of crack initiation and growth in viscoelastic media - I. Theoretical development. Int. J. Fract. 11, 141–159. https://doi.org/10.1007/BF00034721

Schapery, R.A., 1975b. A theory of crack initiation and growth in viscoelastic media II. Approximate methods of analysis. Int. J. Fract. 11, 369–388. https://doi.org/10.1007/BF00033526

Simo, J.C., 1987. On a fully three-dimensional finite-strain viscoelastic damage model:

Formulation and computational aspects. Comput. Methods Appl. Mech. Eng. 60, 153–173. https://doi.org/10.1016/0045-7825(87)90107-1

Slootman, J., Waltz, V., Yeh, C.J., Baumann, C., Göstl, R., Comtet, J., Creton, C., 2020. Quantifying rate-and temperature-dependent molecular damage in elastomer fracture. Phys. Rev. X 10, 041045. https://doi.org/10.1103/PhysRevX.10.041045

Sun, T.L., Kurokawa, T., Kuroda, S., Ihsan, A. Bin, Akasaki, T., Sato, K., Haque, M.A., Nakajima, T., Gong, J.P., 2013. Physical hydrogels composed of polyampholytes demonstrate high toughness and viscoelasticity. Nat. Mater. 12, 932–937. https://doi.org/10.1038/nmat3713

Sun, T.L., Luo, F., Hong, W., Cui, K., Huang, Y., Zhang, H.J., King, D.R., Kurokawa, T., Nakajima, T., Gong, J.P., 2017. Bulk energy dissipation mechanism for the fracture of tough and self-healing hydrogels. Macromolecules 50, 2923–2931. https://doi.org/10.1021/acs.macromol.7b00162

Sun, T.L., Luo, F., Kurokawa, T., Karobi, S.N., Nakajima, T., Gong, J.P., 2015. Molecular structure of self-healing polyampholyte hydrogels analyzed from tensile behaviors. Soft Matter 11, 9355–9366. https://doi.org/10.1039/c5sm01423a

Tang, J., Li, J., Vlassak, J.J., Suo, Z., 2017. Fatigue fracture of hydrogels. Extrem. Mech. Lett. 10, 24–31. https://doi.org/10.1016/j.eml.2016.09.010

Tsunoda, K., Busfield, J.J.C., Davies, C.K.L., Thomas, A.G., 2000. Effect of materials variables on the tear behaviour of a non-crystallizing elastomer. J. Mater. Sci. 35, 5187–5198. https://doi.org/10.1023/A:1004860522186

Venkata, S.P., Cui, K., Guo, J., Zehnder, A.T., Gong, J.P., Hui, C.Y., 2021. Constitutive modeling of strain-dependent bond breaking and healing kinetics of chemical polyampholyte (PA) gel. Soft Matter 17, 4161–4169. https://doi.org/10.1039/d1sm00110h

Wang, J., Cui, K., Zhu, B., Gong, J.P., Hui, C.Y., Zehnder, A.T., 2023. Load transfer between permanent and dynamic networks due to stress gradients in nonlinear viscoelastic hydrogels. Extrem. Mech. Lett. 58, 101928. https://doi.org/10.1016/j.eml.2022.101928

Wang, X., Hong, W., 2012. Delayed fracture in gels. Soft Matter 8, 8171–8178. https://doi.org/10.1039/c2sm25553g

Yeoh, O.H., 1993. Some Forms of the Strain Energy Function for Rubber. Rubber Chem. Technol. 66, 754–771. https://doi.org/10.5254/1.3538343

Zhang, Y., Fukao, K., Matsuda, T., Nakajima, T., Tsunoda, K., Kurokawa, T., Gong, J.P., 2022. Unique crack propagation of double network hydrogels under high stretch. Extrem. Mech. Lett. 51, 101588. https://doi.org/10.1016/j.eml.2021.101588

Zhao, X., 2014. Multi-scale multi-mechanism design of tough hydrogels: Building dissipation into stretchy networks. Soft Matter 10, 672–687. https://doi.org/10.1039/c3sm52272e